Environmental Science and Pollution Research (2022) 29:26425–26448
https://doi.org/10.1007/s11356-021-17549-5

RESEARCH ARTICLE

Batch and continuous adsorption of Cu(II) and Zn(II) ions from aqueous solution on bi-functionalized sugarcane-based biosorbent

Filipe Simões Teodoro[1] · Liliane Catone Soares[1] · Jefferson Gonçalves Filgueiras[2,3] · Eduardo Ribeiro de Azevedo[2] · Álvaro Javier Patiño-Agudelo[4,5] · Oscar Fernando Herrera Adarme[6] · Luis Henrique Mendes da Silva[4] · Leandro Vinícius Alves Gurgel[1]

Received: 28 July 2021 / Accepted: 11 November 2021 / Published online: 2 December 2021

Abstract

A new one-pot synthesis method optimized by a 2^3 experimental design was developed to prepare a biosorbent, sugarcane bagasse cellulose succinate pyromellitate (SBSPy), for the removal of Cu(II) and Zn(II) from single-component aqueous solutions, in batch and continuous modes. The bi-functionalization of the biosorbent with ligands of different chemical structures increased its selectivity, improving its performance for removing pollutants from contaminated water. The succinate moiety favored Cu(II) adsorption, while the pyromellitate moiety favored Zn(II) adsorption. Sugarcane bagasse (SB) and SBSPy were characterized using several techniques. Analysis by ^{13}C Multi-CP SS NMR and FTIR revealed the best order of addition of each anhydride that maximized the chemical modification of SB. The maximum adsorption capacities of SBSPy for Cu(II) and Zn(II), in batch mode, were 1.19 and 0.95 mmol g^{-1}, respectively. Homogeneous surface diffusion, intraparticle diffusion, and Boyd models were used to determine the steps involved in the adsorption process. Isothermal titration calorimetry was used to assess changes in enthalpy of adsorption as a function of SBSPy surface coverage. Fixed-bed column adsorption of Cu(II) and Zn(II) was performed in three cycles, showing that SBSPy has potential to be used in water treatment. Breakthrough curves were well fitted by the Thomas and Bohart-Adams models.

Keywords Mixed ester · Nuclear magnetic resonance · Isothermal titration calorimetry · Thomas model · Bohart-Adams model

Responsible Editor: Tito Roberto Cadaval Jr

✉ Leandro Vinícius Alves Gurgel
legurgel@ufop.edu.br

[1] Grupo de Físico-Química Orgânica, Departamento de Química, Instituto de Ciências Exatas e Biológicas, Universidade Federal de Ouro Preto, Campus Morro do Cruzeiro, s/nº, Bauxita, Ouro Preto, Minas Gerais 35400-000, Brazil

[2] Instituto de Física de São Carlos, Universidade de São Paulo, Av. Trabalhador São-carlense, 400, São Carlos, São Paulo 13566-590, Brazil

[3] Instituto de Química, Universidade Federal Fluminense, Outeiro de São João Batista, s/n, Niterói, Janeiro 24020-007, Brazil

[4] Grupo de Química Verde Coloidal e Macromolecular, Departamento de Química, Centro de Ciências Exatas e Tecnológicas, Universidade Federal de Viçosa, Av. P. H. Rolfs, s/n°, Viçosa, Minas Gerais 36570-000, Brazil

[5] Instituto de Química, Universidade de São Paulo, Av. Lineu Prestes, 748, Cidade Universitária, São Paulo 05508-000, Brazil

[6] Laboratório de Química Tecnológica e Ambiental, Departamento de Química, Instituto de Ciências Exatas e Biológicas, Universidade Federal de Ouro Preto, Campus Universitário Morro do Cruzeiro, s/nº, Bauxita, Ouro Preto, Minas Gerais 35450-000, Brazil

Abbreviations

$M(II)]_x$	Concentration at time t (x = t), at equilibrium (x = e), or initial (x = i) concentration of Cu(II) or Zn(II)
$\Delta_{ads}G^o$	Change in standard free energy of adsorption (kJ mol^{-1})
$\Delta_{ads}H$	Change in enthalpy of adsorption (kJ mol^{-1})
$\Delta_{ads}S^o$	Change in standard entropy of adsorption (J K^{-1} mol^{-1})
b	Langmuir constant (L mol^{-1})
B	Boyd plot slope
Bi	Biot number
C_x	Metal ion solution concentration at time t (x = t) or equilibrium (x = e) (mmol L^{-1})
D_s	Surface diffusion coefficient (m^2 s^{-1})
$E_{re\text{-}ads}$	Re-adsorption efficiency (%)
HSDM	Homogeneous surface diffusion model
I_e	Ionic strength (mol L^{-1})
IPD	Intraparticle diffusion model
$k_{B\text{-}A}$	Bohart-Adams kinetic rate constant (mL mmol^{-1} min^{-1})
$k_{d,i}$	Intraparticle diffusion coefficient (mmol g^{-1} min$^{-1/2}$) of step i
k_f	Film mass transfer coefficient (m s^{-1})
k_{Th}	Thomas kinetic rate constant (mL mmol^{-1} min^{-1})
n	Sips parameter
$n_{T,COOH}$	Total number of carboxylic acid functions (mmol g^{-1})
pH_{PZC}	Point of zero charge
Py	Pyromellityl
PyA	Pyromellitic dianhydride
θ	Adsorbent surface coverage
q_e	Equilibrium adsorption capacity (mmol g^{-1})
Q_{max}	Maximum adsorption capacity (mmol g^{-1})
$q_{x,M(II)}$	Adsorption capacity at time t (x = t) or at equilibrium (x = e), for Cu(II) or Zn(II) on SBSPy (mmol g^{-1})
R	Gas constant (J mol^{-1} K^{-1})
R^2	Coefficient of determination
R^2_{adj}	Adjusted coefficient of determination
r_H	Hydrated ionic radius (Å)
RSS	Residual sum of squares
S	Succinyl
SA	Succinic anhydride
SB	Sugarcane bagasse
SBPy	Sugarcane bagasse cellulose pyromellitate
SBS	Sugarcane bagasse cellulose succinate
SBSPy	Sugarcane bagasse cellulose succinate pyromellitate
SBSPy-M(II)	Sugarcane bagasse cellulose succinate pyromellitate loaded with Cu (M = Cu) or Zn (M = Zn)
T	Temperature (K or °C)
t	Time
T_2	Transverse relaxation time (s)
t_{SA}	Reaction time with succinic anhydride (h)
$T\Delta_{ads}S^o$	Entropic contribution (kJ mol^{-1})
V	Volume
V	Volumetric flow rate (mL min^{-1})
wg	Weight gain (%)
w_{SBSPy}	Weight of SBSPy (g)
γ_e	Activity coefficient at equilibrium
χ^2_{red}	Reduced chi-square
χ_{SA}	Mole fraction of succinic anhydride
Z_{MTZ}	Length of the mass transfer zone (cm)

Introduction

Water shortages have caused great concern in several countries worldwide. At the same time, water quality has worsened due to the inappropriate discharges of effluents into soils and water bodies, over the years, by industries such as ferrous and non-ferrous metal mining, metal plating, and others (Li et al. 2019). Contamination of soils, groundwater, and surface water bodies with industrial effluents containing toxic metals is a critical environmental problem, since it causes severe adverse effects in ecosystems (Kumar et al. 2019, Salomons et al. 1995, Tang et al. 2019). Although copper and zinc are among the most common potentially toxic metals contained in industrial effluents, they are also essential trace elements for humans and animals. Acute exposure to Cu(II) and Zn(II) can contribute to adverse health issues such as heart and brain diseases, high blood pressure, destruction of red blood cells, and infantilism (Araya et al. 2007, Członkowska et al. 2018, Lu et al. 2005, Taylor et al. 2020).

Biosorption is a promising technique for the removal of toxic metals from effluents, especially because biosorbents can be produced from various agroindustrial wastes. Biosorption can offer flexibility in the operation of water and wastewater treatment plants, allowing the reuse or disposal of treated water, recovery of valuable metal ions, and regeneration of the biosorbent. The ability to regenerate the biosorbent is crucial for the economic viability of water and wastewater treatment plants operating with biosorption as a polishing step (O'Connell et al. 2008, Upadhyay et al. 2021).

The chemical modification of a lignocellulosic biomass, such as sugarcane bagasse (SB) (Harripersadth et al. 2020, Homagai et al. 2010, Júnior et al. 2009, Ramos et al. 2015), to produce a biosorbent able to remove toxic metals from water and wastewater is an attractive way to add value to a

byproduct from agroindustry. The bi-functionalization of the biosorbent using two organic ligands with different physicochemical properties (such as acidity constants) can increase the overall performance of the bioadsorbent in a water or wastewater treatment plant, enabling adsorption in a wider pH range, improved capacity for regeneration, and higher selectivity for the removal of toxic metals. The selectivity of the bioadsorbent can be controlled by introducing different proportions of two organic ligands in its structure.

Therefore, the aim of this study was to synthesize a mixed ester of sugarcane bagasse cellulose, using succinic and pyromellitic anhydrides, according to a new synthesis method employing a one-pot reaction. The evidence of chemical modification was provided by elemental C, H, and N analysis, thermogravimetric analysis (TGA), X-ray diffraction (XRD), and Fourier transform infrared (FTIR) spectroscopy. The use of ^{13}C multiple cross-polarization solid-state nuclear magnetic resonance (^{13}C Multi-CP SS NMR) enabled quantification of the number of succinyl (S) and pyromellityl (Py) units introduced into the SB structure. The performance of the synthesized biosorbent was evaluated using the adsorption of Cu(II) and Zn(II) ions from single-component spiked aqueous solutions, in batch and continuous (fixed-bed column) modes. To this end, a 2^3 experimental design was used to investigate the effects of the reaction parameters temperature (T), mole fraction of succinic anhydride (χ_{SA}), and reaction time (t) with each carboxylic acid anhydride, on the capacity for adsorption of Cu(II) and Zn(II). The ability to regenerate and reuse the biosorbent in batch and continuous processes was also evaluated. The thermodynamics of adsorption was investigated, considering the changes in standard free energy, enthalpy, and entropy, and their individual contributions to the adsorption process. The adsorption kinetics was investigated using the homogeneous surface diffusion model (HSDM).

Materials and methods

Materials

Pyromellitic dianhydride (PyA, ≥ 97.0%, MW = 218.12 g mol^{-1}) and succinic anhydride (SA, MW = 100.07 g mol^{-1}) were purchased from Sigma-Aldrich. $ZnSO_4{\cdot}7H_2O$, $CuSO_4{\cdot}5H_2O$, HNO_3 (65 wt.% in water), and NaCl were purchased from Synth (Brazil). The other materials and chemicals used were the same as reported previously (Elias et al. 2019, Almeida et al. 2019). Raw SB (45.5 ± 0.3% cellulose, 30.6 ± 0.5% hemicelluloses, and 23.8 ± 0.8% lignin) (Elias et al. 2019) was kindly donated by the Jatiboca sugar and ethanol mill (Urucânia, Minas Gerais, Brazil).

Preliminary tests for chemical modification of raw SB with SA and PyA

The chemical modification of raw SB (32 mesh, 0.500 mm) with SA and PyA was performed using a one-pot reaction method. Preliminary synthesis tests were carried out to evaluate the reactivity of the two anhydrides in the presence of each other, as well as to determine the best order of addition of each anhydride into the reaction medium. To this end, SA and PyA were added separately to the reaction medium, with the former carboxylic acid anhydride added at the beginning of the reaction and the latter added during the course of the reaction, and vice-versa.

Raw SB (1.000 g), SA (χ_{SA} = 0.5) or PyA (χ_{PyA} = 0.5), anhydrous pyridine (Py, 7.5 mL), and anhydrous *N*,*N*-dimethylacetamide (DMA, 7.5 mL) were added to a 50-mL double-neck round-bottom flask fitted with a reflux condenser, containing a drying tube filled with anhydrous $CaCl_2$ powder, and a solids addition funnel closed with a rubber folding-skirt stopper. The flask was immersed in a canola oil bath (100 °C) placed on a heating plate (Model PC-420D, Corning®) and was stirred at 300 rpm for 3 h, followed by addition of SA (χ_{SA} = 0.5) or PyA (χ_{PyA} = 0.5). A ratio of carboxylic acid anhydrides (SA plus PyA) to raw SB of 4.0 g g^{-1} was used. After a further 3 h, the reaction was completed. The material synthesized using the addition of SA first was denoted SBSPy, while the material synthesized with the addition of PyA first was denoted SBPyS.

After cooling the flask to room temperature, the mixture was poured into a glass Büchner funnel (150 mL, porosity 1) and the solid (SBSPy or SBPyS) was rinsed, under reduced pressure, with ethyl alcohol (95%, 50 mL), distilled water (100 mL), aqueous NaOH solution (0.01 mol L^{-1}, 100 mL), distilled water (100 mL), aqueous HCl solution (0.01 mol L^{-1}, 100 mL), distilled water (100 mL), ethyl alcohol (99.8%, 50 mL), and 2-propanone (50 mL). The SBSPy or SBPyS was dried at 85 °C for 1.5 h in an oven (Model Orion-515, Fanem).

Evaluation of the synthesis of SBSPy using a 2^3 experimental design

The best synthesis condition for SBSPy was determined using a 2^3 experimental design, with T, t_{SA}, and χ_{SA} as independent variables (*IV*s), and the equilibrium adsorption capacities for Cu(II) ($q_{e,Cu}$) and Zn(II) ($q_{e,Zn}$) as dependent variables (*DV*s). The statistical analyses were performed with a confidence level of 95%, using the 2-way interaction model and residual sum of squares (*RSS*) to estimate the standard errors. The processing of the experimental data was performed using Statistica® v. 12.0 software (StatSoft Inc., USA). For determination of the best SBSPy synthesis condition, SA was added before PyA, based on the results of the

preliminary synthesis experiments ("Preliminary tests for chemical modification of raw SB with SA and PyA" section). The other synthesis procedures used were those described in the "Preliminary tests for chemical modification of raw SB with SA and PyA" section.

The desirability tool of the Statistica® software was used to predict the best synthesis condition that maximized the values of both $q_{e,Cu}$ and $q_{e,Zn}$. In this procedure, the values of the responses $q_{e,Cu}$ and $q_{e,Zn}$ were set to 1.0. Scores of 0.0 and 1.0 obtained using the desirability tool indicate undesirable and desirable values, respectively, for the responses under optimization.

Characterization of raw SB and SBSPy

Before characterization analyses of raw SB and SBSPy, the materials were rinsed under reduced pressure with 2-propanone in a glass Büchner funnel (150 mL, porosity 1), dried in an oven at 85 °C for 1 h and cooled in a desiccator. The value of the total number of carboxylic acid functions ($n_{T,COOH}$) was determined for both materials, using the method described by Teodoro et al. (2016). The methods used to characterize raw SB and SBSPy by FTIR, point of zero charge (pH_{PZC}), and elemental analysis of C, H, and N were the same as described by Pereira et al. (2020). The characterizations of the materials by TGA, XRD, specific surface area (Brunauer-Emmett-Teller (BET) method), and pore size distribution (Barrett-Joyner-Halenda (BJH) method) measurements were as described by Teodoro et al. (2016).

^{13}C Multiple cross-polarization solid-state nuclear magnetic resonance (^{13}C Multi-CP SS NMR) spectroscopy

Estimation of the numbers of succinyl (S) and pyromellityl (Py) units introduced into the SBSPy and SBPyS structures was performed using ^{13}C Multi-CP SS NMR spectroscopy. NMR spectra of raw SB, SBSPy, and SBPyS were acquired with a Bruker spectrometer (Model Avance 400) equipped with a 4-mm magic angle spinning (MAS) double-resonance probe, operating at frequencies of 100.5 MHz (^{13}C) and 400.0 MHz (^{1}H). Further information about other procedures used and the analysis conditions can be found in the studies of Elias et al. (2019) and Almeida et al. (2019).

The estimation of the numbers of succinyl and pyromellityl units introduced into the SB structure was performed by normalizing the NMR spectra of raw SB and SBSPy or SBPyS using the signal areas corresponding to the anomeric carbon atom (C-1) of the cellulose. The spectral areas corresponding to regions A (24–40 ppm) and B (120–140 ppm) were then calculated for the raw SB, SBSPy, and SBPyS spectra. Signals related to the methylene carbons of succinyl units were expected to appear in region A, while those related to aromatic carbons of pyromellityl units were expected to appear in region B, together with signals for some of the aromatic carbons of lignin. In order to obtain the spectral area corresponding to pyromellityl in region B of the SBSPy or SBPyS spectrum, without considering the lignin contribution, the area calculated for the SBSPy or SBPyS spectrum was subtracted from the corresponding area for the raw SB spectrum. With this normalization and subtraction procedure, the spectral areas obtained from the regions A and B (subtracted from the area of the raw SB spectrum) became proportional to the number of carbon atoms of succinyl and pyromellityl units, respectively, introduced into SBSPy or SBPyS, relative to the number of C-1 carbon atoms per cellobiose unit (two β-D-anhydroglucose units (AGU) linked by a β(1→4) glycosidic bond). Further procedures used for calculation of the numbers of succinyl and pyromellityl units introduced into the SB structure were those reported by Elias et al. (2019) and Almeida et al. (2019).

NMR relaxometry

The samples of raw SB and SBSPy were first dried at 80 °C for 24 h, under reduced pressure of 800 mmHg. The samples were then soaked with DMA and kept under reduced pressure overnight. The excess DMA was removed by centrifugal filtration for 1 min using a 0.45-µm nylon membrane (Spin-X, Corning® Costar®) and a relative centrifugal force of 200 × *g*.

All the measurements were performed using a Bruker Minispec MQ-20 spectrometer operating with a 0.5 T magnetic field (^{1}H Larmor frequency of 20 MHz), employing a CPMG (Carr-Purcell-Meiboom-Gill) sequence. The acquisition parameters were set to 25,000 echoes, echo time of 100 µs, and recycle delay of 10 s. For each sample, the T_2 distributions were obtained using a numerical inverse Laplace transform (ILT) procedure (Borgia et al. 1998, Provencher 1982). Deconvolution of the T_2 distribution with three log-Gaussian functions enabled isolation of the contribution of each component of the distribution. The experiments were carried out in duplicate and the ILT was performed on the CPMG decay given by the average of the normalized data for each measurement.

The interaction between the pore surface and the ^{1}H nuclear spins of a fluid speed up the relaxation of the fluid confined inside the pore, according to a phenomenon known as surface relaxation (Meng & Ragauskas 2014). This effect allows the extraction of information about the pore space geometry, since the observed transverse relaxation rate, $1/T_2$, is directly proportional to the surface to volume ratio of the pore. Hence, the T_2 distribution of a fluid confined on a given porous system qualitatively reflects the pore size

distribution. At the fast diffusion limit, the relation between T_2 and pore size is given by Eq. (1) (Brownstein & Tarr 1979, Capitani et al. 2012).

$$\frac{1}{T_2} = \rho\left(\frac{S}{V}\right) \quad (1)$$

where ρ is the surface relaxivity, which depends on the porous medium and is usually unknown, and S and V are the pore surface area and volume, respectively. Both the pore size distribution and the differences in fluid mobility within the pores affect the T_2 distribution.

Scanning electron microscopy

The morphological aspects of the raw SB and SBSPy surfaces were examined by scanning electron microscopy (SEM), using a Tescan/Oxford scanning electron microscope (Model Vega3 SB) equipped with a tungsten filament and a secondary electron detector. Prior to analysis, the raw SB and SBSPy (32-mesh, 0.500 mm) were mounted separately on carbon graphite tapes adhered to aluminum stubs, followed by coating with a thin layer of gold using a Quorum modular high-vacuum coater (Model Q150R ES).

Batch adsorption experiments

Assays of the single-component adsorption of Cu(II) and Zn(II) on SBSPy were performed (in batch mode) to evaluate the effects of solution pH, time, and initial Cu(II) or Zn(II) concentration. Buffer solutions were used to control the solution pH during the adsorption experiments. All the buffered Cu(II) and Zn(II) solutions were prepared using deionized water from a Milli-Q system (Millipore®). The experimental conditions used in the adsorption experiments are summarized in Table 1. Erlenmeyer flasks (250 mL) containing samples of SBSPy weighed into cylindrical glass bottles (1.8 mm H × 2.2 mm OD) were stirred at 130 rpm in an orbital shaker-incubator (Model MA-830, Marconi). All the experiments were performed in duplicate, at 25 °C.

At the end of the adsorption experiment, the spent SBSPy was separated from the liquid phase by single filtration, using JP-41 filter paper, and the concentration of Cu(II) (λ = 324.8 nm) or Zn(II) (λ = 213.9 nm) was determined using a flame atomic absorption spectrophotometer (FAAS) (Model SpectrAA 50B, Varian®).

The q_x value of the SBSPy for each cation was obtained using Eq. (2):

$$q_x = \frac{\left([M(II)]_0 - [M(II)]_x\right)_{M(II)} V_{M(II)}}{w_{SBSPy}} \quad (2)$$

where q_x (mmol g^{-1}) is the SBSPy adsorption capacity at time t (x = t) or at equilibrium (x = e), $V_{M(II)}$ (L) is the volume of M(II) (M = Cu or Zn) solution, the term $([M(II)]_0 - [M(II)]_x)_{M(II)}$ (mmol L^{-1}) is the difference between the initial M(II) concentration and the concentration of M(II) at time t or at equilibrium e, and w_{SBSPy} (g) is the weight of SBSPy.

The data for adsorption as a function of time were modeled using the homogeneous surface diffusion model (HSDM) (Worch 2012), the intraparticle diffusion (IPD) model (Weber & Morris 1963), and the Boyd model (Boyd et al. 1947). The data for adsorption as a function of the initial Cu(II) or Zn(II) concentration were modeled using the Langmuir (Langmuir 1918) and Sips (Sips 1948) models. The equations used to fit the adsorption data can be found in the Online Resources.

Table 1 Conditions used in the adsorption, desorption, and re-adsorption experiments

Experiment type[a]	SBSPy dosage / g L^{-1}	Contact time/ min	pH[b]	Solution concentration/mmol L^{-1}
Solution pH	0.2	600	2-5.5	0.79 Cu(II) 0.79 Zn(II)
Kinetics	0.2	2–600	5.5	0.79 Cu(II) 0.79 Zn(II)
Isotherm	0.2	120 Cu(II) 180 Zn(II)	5.5	0.002-2.895 Cu(II) 0.016-3.201 Zn(II)
Adsorption / re-adsorption	0.2	360	5.5	0.79 Cu(II) 0.79 Zn(II)
Desorption	1.0	25	~0.3	505 HNO_3

[a]All experiments were performed at 25 °C, under agitation of 130 rpm

[b]Buffer solution: pH 2–3.5 (α-chloroacetic acid/sodium α-chloroacetate); pH 4–5.5 (acetic acid/sodium acetate)

Batch desorption and re-adsorption experiments

The potential to reuse the spent SBSPy was evaluated in desorption and re-adsorption experiments. Erlenmeyer flasks (125 mL) containing samples of SBSPy, SBSPy-Cu(II), or SBSPy-Zn(II) weighed into cylindrical glass bottles (1.8 mm H × 2.2 mm OD) were stirred at 130 rpm and 25 °C in an orbital shaker-incubator (Model MA-830, Marconi). The efficiencies of desorption (E_{des}) and re-adsorption ($E_{re\text{-}ads}$) were calculated from mass balance equations, as described by Almeida et al. (2016) and Teodoro et al. (2016). The conditions of the SBSPy reuse experiments are summarized in Table 1. The other procedures were those described in the "Batch adsorption experiments" section. The assays of desorption and re-adsorption were both performed in triplicate.

Evaluation of adsorption thermodynamics

The changes in the enthalpy of adsorption ($\Delta_{ads}H$) were determined by isothermal titration calorimetry (ITC). The values of $\Delta_{ads}H$ as a function of SBSPy surface coverage (θ), for adsorption of Cu(II) or Zn(II), were measured using a nanocalorimeter (Model TAM III, TA Instruments®) equipped with two 4-mL calorimetry cells. The reference cell was filled with 2.7 mL of acetic acid/sodium acetate buffer solution (pH 5.5). The same volume was added to the sample cell containing 0.0100 ± 0.0001 g of SBSPy. The suspension in the sample cell was stirred continuously, using a propeller stirrer at 180 rpm. After thermal equilibrium had been reached and the liquid phase was degassed, injections of 15 µL of Cu(II) or Zn(II) solution (47 mmol L^{-1} Cu(II) or 38 mmol L^{-1} Zn(II)), prepared in the same buffer, were performed at 35-min intervals, using a 500-µL Hamilton syringe controlled by a piston pump. All the calorimetric titrations were performed at 25.00000 ± 0.00001 °C, in duplicate. The other experimental conditions were as described by Pereira et al. (2020).

The contribution of Cu(II) or Zn(II) dilution enthalpy to the overall adsorption process was determined by ITC measurements without the addition of SBSPy. The $\Delta_{ads}H$ values for different amounts of Cu(II) or Zn(II) adsorbed on SBSPy were calculated using Eq. (3):

$$\Delta_{ads}H = \frac{\sum_{i=1}^{N}\left(q_{i,int} - q_{i,del}\right)}{\sum_{i=1}^{N} n_i} \tag{3}$$

where ($q_{i,int} - q_{i,dil}$) (kJ) is the difference between the absorbed or released heat due to interaction after each injection i in the sample cell, for the ITC experiments performed with SBSPy ($q_{i,int}$) or without SBSPy ($q_{i,dil}$), respectively, and n_i (mol) is the amount of Cu(II) or Zn(II) adsorbed on SBSPy. The calculation of the n_i values was as described by Pereira et al. (2020).

The calculation of the change in standard free energy ($\Delta_{ads}G°$) for adsorption of Cu(II) or Zn(II) on SBSPy was performed according to the approach described by Liu (2009), as shown in Eq. (4):

$$\Delta_{ads}G° = -RT\ln\left[\frac{b}{\gamma_e}\left(1\text{molL}^{-1}\right)\right] \tag{4}$$

where T (K) is the absolute temperature, R (J mol^{-1} K^{-1}) is the gas constant, b (L mol^{-1}) is the Langmuir constant, and γ_e is the activity coefficient of the Cu(II) or Zn(II) solution at equilibrium (at 25 °C).

Since the concentration of the Cu(II) or Zn(II) solution affected the γ_e value, a correction of the value was required. The extended Debye-Hückel law (Huckel & Debye 1923) (Eq. (5)) was used for this purpose, as follows:

$$\log\gamma_e = \frac{-Az^2\sqrt{I_e}}{1 + B\alpha\sqrt{I_e}} \tag{5}$$

where I_e (mol L^{-1}) is the ionic strength of the Cu(II) or Zn(II) solution, z is the charge of Cu(II) or Zn(II), α is the effective diameter of the Cu(II) or Zn(II) ion (6 Å) (Fetter 2018), and A and B are empirical constants with values of 0.5085 and 0.3281 at 25 °C in water, respectively (Garrels & Christ 1965).

The $\Delta_{ads}G°$ parameter (Eq. (6)) is a result of enthalpic and entropic contributions to the adsorption system under study. The change in the standard enthalpy of adsorption, $\Delta_{ads}H°$, was determined from a plot of $\Delta_{ads}H$ against C_e, extrapolating $C_e \rightarrow 0$ (Figure not shown). The change in the standard entropy of adsorption, $\Delta_{ads}S°$, was determined from Eq. (6).

$$\Delta_{ads}G° = \Delta_{ads}H° - T\Delta_{ads}S° \tag{6}$$

Continuous adsorption on a fixed-bed column

The continuous adsorption experiments were performed using three adsorption-desorption cycles, according to the methods described by Almeida et al. (2019). The experimental conditions for continuous adsorption on a fixed-bed column were based on the results obtained in the batch adsorption studies of Cu(II) and Zn(II) on SBSPy ("Batch adsorption experiments" and "Batch desorption and re-adsorption experiments" sections), as well as on the results reported by Xavier et al. (2018), who optimized the continuous adsorption of Co(II), Cu(II), and Ni(II) on sugarcane bagasse chemically modified with trimellitic anhydride (TA). In the first cycle, buffered metal ion solution (1.4 mmol L^{-1}, pH 5.5, 25 °C) was pumped at a flow rate of 2.35 mL min^{-1} for 440 min for Cu(II) and 420 min for Zn(II). The HNO_3 desorption solution (0.505 mol L^{-1}, 25 °C) was then percolated through the bed for 10 min, at a flow rate of

10 mL min^{-1}. Deionized water was percolated through the bed after the adsorption step, to eliminate all the cations not adsorbed on SBSPy, and after the desorption step, to remove excess HNO_3 solution.

Aliquots of the effluent to the column were collected at specific times, with quantification of the Cu(II) or Zn(II) concentrations by FAAS ("Batch adsorption experiments" section), in order to obtain the breakthrough curves. The adsorption capacity of SBSPy packed into the column, for a given operating time, was calculated from the area under the curve, according to Eq. (7):

$$Q/\mathrm{mmol\,g^{-1}} = \frac{C_0 \dot{V}}{1000 w_{\mathrm{SBSPy}}} \int_0^t \left(1 - \frac{C_t}{C_0}\right) dt \tag{7}$$

where Q is the adsorption capacity of the SBSPy (mmol g^{-1}), C_0/C_t is the normalized Cu(II) or Zn(II) concentration, w_{SBSPy} is the weight of SBSPy packed into the column (g), and V is the volumetric flow rate of the fluid phase (mL min^{-1}). The maximum adsorption capacity (Q_{max}) of the bed was reached when C_t was equal to C_0.

The effective use of the bed (H) was the effective height of the bed used for Cu(II) or Zn(II) adsorption until the breakthrough point. The H value was calculated using Eq. (8):

$$H/cm = \left(\frac{q_{t_b}}{q_{t_e}}\right) Z \tag{8}$$

where H is the effective use of the bed (cm), q_{tb} and q_{te} (mmol) are the amounts of Cu(II) or Zn(II) adsorbed on SBSPy until the breakthrough time (t_b) and until the exhaustion time (t_e), which were obtained from the breakthrough curve at $C_t/C_0 = 0.05$ and at $C_t/C_0 = 0.95$, respectively, and Z is the bed height ($Z = 3.0$ cm).

The efficiency of the adsorption process (EAP) in a fixed-bed column was calculated using Eq. (9):

$$EAP/\% = \left(\frac{q_{t_e}}{q_{\mathrm{M(II)}}}\right) \times 100 \tag{9}$$

where EAP is the efficiency of the adsorption process (%) and $q_{\mathrm{M(II)}}$ is the total amount of Cu(II) or Zn(II) fed into the column (mmol).

The length of the mass transfer zone (Z_{MTZ}) was calculated using Eq. (10):

$$Z_{\mathrm{MTZ}}/cm = \left(1 - \frac{t_b}{t_e}\right) Z \tag{10}$$

where Z_{MTZ} is the length of the mass transfer zone (cm).

The E_{des} value for each cycle was calculated as shown in Eq. (11):

$$E_{\mathrm{des}}/\% = \left(\frac{\dot{V} \int_0^t (C_t)\, dt}{Q_{\mathrm{max}} w_{\mathrm{SBSPy}}}\right) \times 100 \tag{11}$$

where C_t is the metal ion concentration (mmol mL^{-1}) in the desorption solution at time t.

The $E_{\mathrm{re\text{-}ads}}$ value was determined considering that the first cycle had 100% of the Q_{max} value of the bed. The breakthrough curves were modeled using the Thomas (Thomas 1944), Bohart-Adams (Bohart & Adams 1920), and instantaneous local equilibrium (ILE) (Georgin et al. 2020) models, using a computational routine implemented in MATLAB® 2016a (MathWorks Inc.), with a genetic algorithm function (Chu 2010, Xavier et al. 2018) employed to find the global minimum (See the Online Resources).

Results and discussion

For the introduction of both succinyl and pyromellityl units into the SB structure by a one-pot reaction, exploratory synthesis experiments were performed to assess which carboxylic acid anhydride should be added first to maximize the chemical modification of raw SB. Subsequently, having defined the best order of addition of SA and PyA, the chemical modification of raw SB with SA and PyA was evaluated employing a 2^3 experimental design to investigate the effects of the synthesis parameters T, t_{SA}, and χ_{SA} on the values of $q_{\mathrm{e,Cu}}$ and $q_{\mathrm{e,Zn}}$.

Exploratory experiments for the synthesis of SBSPy

The FTIR spectra of raw SB, SBSPy (SA added first), SBPyS (PyA added first), and raw SB modified with SA only (SBS) and with PyA only (SBPy) are presented in Figure 1a. All the chemically modified materials showed an intense band in the region of 1720–1740 cm^{-1}, which was related to stretching of the carbonyl ester group. A weak band related to stretching of the carbonyl ester group was also present at 1735 cm^{-1} in the raw SB spectrum, attributed to the acetyl groups in hemicelluloses. The bands related to stretching of the carbonyl ester group in SBSPy, SBS, SBPyS, and SBPy are highlighted in Figure 1b. For SBPy (Figure 1b), the band related to the carbonyl ester group of the pyromellityl unit (conjugated carbonyl) appeared centered at 1729 cm^{-1}. As expected, conjugation of the carbonyl group with the phenyl group shifted the carbonyl band stretching to a lower frequency (Pavia et al. 2009). For SBS (Figure 1b), the band related to the carbonyl ester group of the succinyl unit (unconjugated carbonyl) appeared centered at 1738 cm^{-1}. In the IR spectrum of SBSPy (Figure 1b), where SA was added

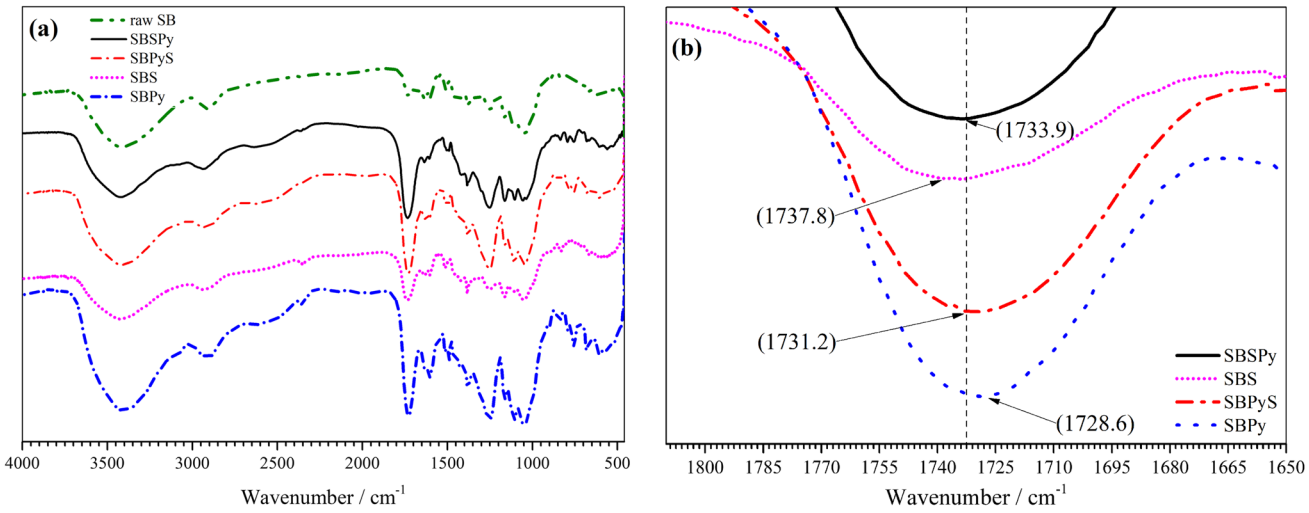

Figure 1 FTIR spectra of **a** raw SB, SBSPy (SA added first), SBPyS (PyA added first), SBS (SA added only), and SBPy (PyA added only), from 500 to 4000 cm^{-1}, and **b** SBSPy, SBS, SBPyS, and SBPy, from 1650 to 1809 cm^{-1} (1% w w^{-1} of sample in KBr)

first, the band related to the carbonyl ester group was shifted to a lower wavenumber (1734 cm^{-1}), compared to its position in the spectrum of SBS (1738 cm^{-1}), due to the introduction of pyromellityl units in SBSPy. In addition, in the spectrum of SBPyS (Figure 1b), where PyA was added first, the band related to the carbonyl ester group was shifted to a higher wavenumber (1731 cm^{-1}), compared to its position in the IR spectrum of SBPy (1729 cm^{-1}), due to the introduction of succinyl units in SBPyS. As expected, the ratio between the pyromellityl (PyA) units and succinyl (SA) units introduced in SBPyS and SBSPy affected the position of the carbonyl ester band. These results suggested that the PyA-to-SA ratio in SBSPy ($\nu C{=}O_{ester}$ shifted from 1738 cm^{-1} (SBS) to 1734 cm^{-1} (SBSPy)) was lower than in SBPyS ($\nu C{=}O_{ester}$ shifted from 1738 cm^{-1} (SBS) to 1731 cm^{-1} (SBPyS)). However, FTIR analysis was unable to provide accurate information on the numbers of succinyl and pyromellityl units introduced in SBSPy and SBPyS. Therefore, the ^{13}C Multi-CP SS NMR technique was used for this purpose.

The ^{13}C Multi-CP SS NMR spectra of raw SB, SBSPy (SA added first), and SBPyS (PyA added first) are presented in Figure 2. The use of the Multi-CP excitation method (Bernardinelli et al. 2015) enabled the acquisition of more quantitative ^{13}C NMR spectra (Almeida et al. 2019, Elias et al. 2019). The introduction of PyA and SA into the SB structure was confirmed by the appearance of signals related to the aromatic carbons of the pyromellityl unit (region B, 120-140 ppm) and the methylene carbons of the succinyl unit (region A, 24–40 ppm) (Figure 2), respectively. Using the approach described in "^{13}C Multiple cross-polarization solid-state nuclear magnetic resonance (^{13}C Multi-CP SS NMR) spectroscopy" section, the numbers of succinyl and pyromellityl units grafted to each cellobiose unit

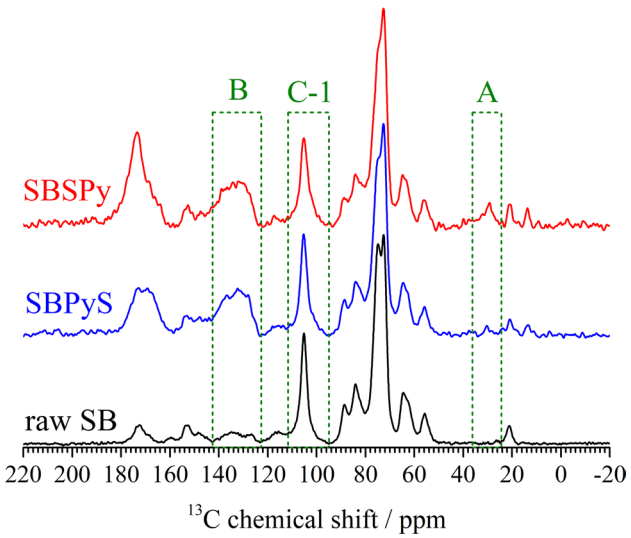

Figure 2 ^{13}C Multi-CP SS NMR spectra of raw SB, SBSPy (SA added first), and SBPyS (PyA added first).

were calculated for SBPyS and SBSPy. It was found that 0.21 ± 0.03 succinyl units and 0.34 ± 0.05 pyromellityl units were grafted to each cellobiose unit in SBPyS, while 0.27 ± 0.03 succinyl units and 0.35 ± 0.05 pyromellityl units were grafted to each cellobiose unit in SBSPy. In addition, these results confirmed that more succinyl units were introduced into the SB structure when SA was added first. This was in agreement with the values obtained from the FTIR spectra of SBSPy (PyA-to-SA ratio of 1.30) and SBPyS (PyA-to-SA ratio of 1.62). These results also suggested that a way to introduce more succinyl and pyromellityl units into the SB structure was to add SA to the reaction medium first.

Therefore, the subsequent synthesis studies were carried out with the addition of SA first.

Evaluation of the effect of synthesis conditions on the adsorption capacity of SBSPy for Cu(II) and Zn(II)

A 2^3 factorial design was used to evaluate the effect of the synthesis conditions (t_{SA}, T, and χ_{SA}) on the values of $q_{e,Cu}$ and $q_{e,Zn}$. The experimental conditions used in the factorial design are shown in Table 2, together with the values of $q_{e,Cu}$ and $q_{e,Zn}$ obtained experimentally. The levels of the independent variables were based on synthesis experiments described elsewhere (Ramos et al. 2015, 2016). Pareto charts of the standardized effects can be found in the Online Resources (Figure S1a–b). The variable T had significant positive effects on $q_{e,Cu}$ (6.743) and $q_{e,Zn}$ (7.337), indicating that the use of T at the higher level for the synthesis of SBSPy favored the adsorption of both metal ions. For Cu(II) adsorption, the interactions between t_{SA} and χ_{SA} (− 3.614) and between T and χ_{SA} (3.496) also had statistical significance. The marginal means plots for $q_{e,Cu}$ are available in the Online Resources (Figure S2a–b). These plots allowed evaluation of the significant interactions for maximizing the $q_{e,Cu}$ value. If the lower level of t_{SA} was applied, the use of χ_{SA} at the higher level was needed to maximize the $q_{e,Cu}$ value. Regarding the interaction between T and χ_{SA}, the use of both variables at the higher level favored the $q_{e,Cu}$ value.

For Zn(II) adsorption, all the variables were statistically significant, with a positive effect of T (7.337) and negative effects of t_{SA} (− 9.656) and χ_{SA} (− 6.157) on the $q_{e,Zn}$ value. Therefore, higher $q_{e,Zn}$ values were obtained using the variables t_{SA} and χ_{SA} at the lower levels and the variable T at the higher level. The interactions of t_{SA} and χ_{SA} (4.842), T and χ_{SA} (− 6.965), and t_{SA} and χ_{SA} and T (− 6.090) were also statistically significant. The marginal means plots for $q_{e,Zn}$ are available in the Online Resources (Figure S3a–c). For all the interactions, higher T levels led to higher $q_{e,Zn}$ values. In addition, the interaction between t_{SA} and χ_{SA} indicated that the lower levels of t_{SA} and χ_{SA} favored higher $q_{e,Zn}$ values.

The results suggested that the use of higher χ_{SA} levels increased the $q_{e,Cu}$ value, while the use of lower χ_{SA} levels (higher amounts of PyA) favored the $q_{e,Zn}$ value. This indicated possible preference of the metal ions for specific adsorption sites. This preference could be explained by the hard and soft acids and bases (HSAB) theory of Pearson (1963). The principle of the HSAB theory suggests that soft acids bind to soft bases, while hard acids bind to hard bases. The hardness and softness of acids and bases is related to the size of the species and their polarizability (Pearson 1963). Cu(II) and Zn(II) are considered borderline Lewis acids, so they can form stable complexes with both soft and hard bases (Pearson 1968). In addition, the electronegativities of Cu(II) and Zn(II) are 1.90 and 1.65, respectively, on the Pauling scale (Haynes et al. 2014). The active adsorption sites introduced on the surface of SBSPy were carboxylate groups that tend to behave as hard bases, although the negatively charged oxygen atom of the carboxylate ion has one of its lone electron pairs involved in resonance, which increases the delocalization of the negative charge (Pearson 1968). On the other hand, the negative charge of the carboxylate ion cannot be delocalized into the pyromellityl group by resonance. However, the other carboxyl functions bonded to the aromatic ring act as electron-withdrawing groups, due to both the inductive effect and the resonance effect, which increases the stability of the conjugated base (the carboxylate ion). This increases the acidity of at least two carboxylic acid groups ($pK_{a,1} = 1.92$, $pK_{a,2} = 2.87$, $pK_{a,3} = 4.49$, and $pK_{a,4} = 5.63$, in water at 25 ºC) (Dean & Lange 1999) of pyromellitic acid (a tetracarboxylic acid), compared to a

Table 2 Experimental conditions and responses obtained for the synthesis of SBSPy using a 2^3 experimental design

Experiment	Independent variable						Dependent variable	
	Uncoded variable			Coded variable			Response	
	T/°C	t_{SA}/h	χ_{SA}	T/°C	t_{SA}/h	χ_{SA}	$q_{e,Zn(II)}$/mmol g^{-1}	$q_{e,Cu(II)}$/mmol g^{-1}
1	50.0	1.0	0.2	-1	-1	-1	0.72 ± 0.03	0.73 ± 0.01
2	100.0	1.0	0.2	+1	-1	-1	0.90 ± 0.01	0.86 ± 0.02
3	50.0	5.0	0.2	-1	+1	-1	0.41 ± 0.02	1.00 ± 0.01
4	100.0	5.0	0.2	+1	+1	-1	0.71 ± 0.01	1.14 ± 0.02
5	50.0	1.0	0.8	-1	-1	+1	0.54 ± 0.01	0.82 ± 0.02
6	100.0	1.0	0.8	+1	-1	+1	0.700 ± 0.003	1.281 ±0.002
7	50.0	5.0	0.8	-1	+1	+1	0.610 ± 0.001	0.82 ± 0.02
8	100.0	5.0	0.8	+1	+1	+1	0.46 ± 0.01	1.22 ± 0.01
9(C)	75.0	3.0	0.5	0	0	0	0.598 ± 0.007	1.05 ± 0.02
10(C)	75.0	3.0	0.5	0	0	0	0.599 ± 0.005	1.05 ± 0.02
11(C)	75.0	3.0	0.5	0	0	0	0.61 ± 0.02	1.05 ± 0.02

saturated aliphatic dicarboxylic acid such as succinic acid ($pK_{a,1}$ = 4.21 and $pK_{a,2}$ = 5.64, in water at 25 ºC) (Dean & Lange 1999), which has the electron-withdrawing inductive effect from an adjacent carboxyl group to another separated by only two methylene groups. Therefore, metal ions classified as softer tend to bind preferentially to the carboxylate functions of the pyromellitate group, since the negative charges of the carboxylate ions are more delocalized in this group, compared to the succinate group. Consequently, Zn(II), which is slightly softer than Cu(II), would be expected to have greater affinity for the pyromellitate group, whereas Cu(II) should have greater affinity for the succinate group.

As the main objective of this study was to synthesize an adsorbent able to remove both metal ions from aqueous solutions, the results obtained using the 2^3 experimental design indicated that the best synthesis condition should use the higher T level (100.0 ºC) and the lower t_{SA} level (1.0 h). For the variable χ_{SA}, the higher χ_{SA} level favored Cu(II) adsorption, while the lower χ_{SA} level favored Zn(II) adsorption. Therefore, the results suggested that the use of higher amounts of SA in the synthesis of SBSPy increased $q_{e,Cu}$, while the use of higher amounts of PyA favored $q_{e,Zn}$, indicating a possible preference of the metal ions for specific adsorption sites, as discussed previously.

The desirability tool of the Statistica® software was used to determine the best condition for synthesis of SBSPy that provided the highest values of $q_{e,Cu}$ and $q_{e,Zn}$. The profiles for the predicted values and desirability are available in the Online Resources (Figure S4). This analysis included maximization of the values of both $q_{e,Cu}$ and $q_{e,Zn}$ ("Evaluation of the synthesis of SBSPy using a 2^3 experimental design" section). The desirability profile indicated that the chemical modification of raw SB with SA and PyA in a one-pot reaction should be carried out using the following reaction conditions: T = 100.0 ºC, t_{SA} = 1.0 h, and χ_{SA} = 0.62. A scheme for the synthesis of SBSPy using the best reaction condition is shown in Figure 3. For this synthesis condition, the predicted values for $q_{e,Cu}$ and $q_{e,Zn}$ were 1.281 ± 0.003 and 0.90234 ± 0.0006 mmol g^{-1}, respectively.

The condition for synthesis of SBSPy predicted by the desirability tool of the Statistica® software was validated experimentally, obtaining $q_{e,Cu}$ and $q_{e,Zn}$ values of 1.18 ± 0.06 and 0.78 ± 0.09 mmol g^{-1}, respectively. The relative errors for the predicted and experimental values of $q_{e,Cu}$ and $q_{e,Zn}$ were 7.8 and 13.3%, respectively. Therefore, these results demonstrated the robustness of the constructed model.

Characterization of raw SB and SBSPy

The following sections present the characterization of SBSPy, prepared using the desirable reaction condition, considering the parameters wg and $n_{T,COOH}$, together with the results of analyses using FTIR, ^{13}C Multi-CP SS NMR, NMR relaxometry, and SEM. The characterization of SBSPy by XRD and TGA is presented in the Online Resources (Figures S5 and S6).

Results for wg, $n_{T,COOH}$, and analyses by FTIR and ^{13}C Multi-CP SS NMR

The SBSPy synthesized using the desirable reaction condition presented wg of 61.621 ± 0.002% and $n_{T,COOH}$ of 4.21 ± 0.07 mmol g^{-1}. These values were similar to those reported by Elias et al. (2019) for the chemical modification of raw SB with SA and PA (phthalic anhydride), in a one-pot reaction to prepare SBSPh (wg = 60.52%, $n_{T,COOH}$ = 3.51 mmol g^{-1}), and by Almeida et al. (2019) for the chemical modification of raw SB with SA and TA (trimellitic anhydride), in a one-pot reaction to prepare SBST (wg = 73.2%, $n_{T,COOH}$ = 4.67 mmol g^{-1}). It is important to note that the synthesis methods used to prepare SBSPh and SBST were different to the procedure used here to prepare

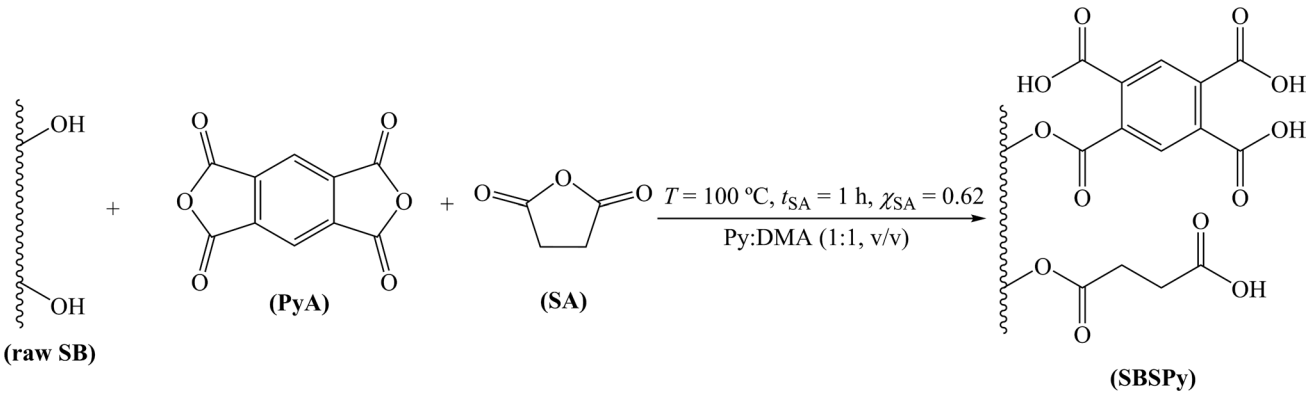

Figure 3 Scheme for the chemical modification of raw sugarcane bagasse (SB) with pyromellitic anhydride (PyA) and succinic anhydride (SA), using the best reaction condition predicted using the desirability tool of Statistica®

SBSPy. The different values of *wg* and $n_{T,COOH}$ for SBSPh, SBST, and SBSPy were related to different numbers of succinyl (0.33) and phthalyl (0.40) units (Elias et al. 2019), succinyl (0.51) and trimellityl (0.59) units (Almeida et al. 2019), and succinyl (0.71) and pyromellityl (0.25) units introduced in SBSPh, SBST, and SBSPy, respectively. In addition, SBSPh and SBST were synthesized by the simultaneous addition of both carboxylic acid anhydrides at the beginning of the one-pot reaction, while in the synthesis of SBSPy, the carboxylic acid anhydrides were added separately. The use of different synthesis methods to prepare SBSPh, SBST, and SBSPy was due to the differences in molecular size and reactivity of PA, TA, and PyA. The total numbers of SA and PA, SA and TA, and SA and PyA units introduced in SBSPh, SBST, and SBSPy were 0.73, 1.1, and 0.96, respectively. It should be noted that the ratios of PA to SA, TA to SA, and PyA to SA units introduced in SBSPh, SBST, and SBSPy were 1.21, 1.16, and 0.35, respectively. Despite the differences in the synthesis conditions used to prepare SBSPh ($T = 100$ ºC, $t = 11$ h, $\chi_{SA} = 0.2$) (Elias et al. 2019), SBST ($T = 100$ ºC, $t = 11$ h, $\chi_{SA} = 0.2$) (Almeida et al. 2019), and SBSPy ($T = 100$ ºC, $t_{SA} = 1$ h, $t_{PyA} = 5$ h, $\chi_{SA} = 0.62$), the results suggested that as the molecular size of the aromatic carboxylic acid anhydride increased, its introduction in the SB structure decreased. As a result, the method used to prepare SBSPy could not be the same as those used to prepare SBSPh and SBST.

The contents of C, H, and N in raw SB and SBSPy were 44.5 ± 0.8% and 47.6 ± 0.3%, 6.0 ± 0.2% and 5.1 ± 0.1%, and 0.2 ± 0.1% and 0.2 ± 0.1%, respectively. These results indicated that the chemical modification of raw SB with SA and PyA was successful, since the theoretical contents of C and H in SA and PyA are 48.01% and 55.07%, and 4.03% and 0.92%, respectively. The contents of C and H in the two carboxylic acid anhydrides could explain the decreased H content and the increased C content in SBSPy, which contained 0.71 succinyl units and 0.25 pyromellityl units.

The FTIR spectra of raw SB and SBSPy are shown in Figure 4. The main evidences of the chemical modification of raw SB with SA and PyA were the appearance of bands at 2631 and 2528 cm^{-1} ($\nu O\text{-}H_{carboxylic\ acid\ dimer}$), 1733 cm^{-1} ($\nu C{=}O_{ester\ and\ carboxylic\ acid}$), 1500 cm^{-1} ($\nu C{=}C_{aromatic\ ring\ (pyromellitic\ ring)}$), 1257 cm^{-1} ($\nu C\text{-}O_{ester}$), and 758 cm^{-1} ($\nu C(sp^2)\text{-}H_{aromatic\ ring\ (pyromellitic\ ring)}$) (Almeida et al. 2019, Elias et al. 2019, Pavia et al. 2009).

The ^{13}C Multi-CP SS NMR spectra of raw SB and SBSPy are shown in Figure 5a. The characteristic signals of the major constituents of raw SB (cellulose, hemicelluloses, and lignin) were assigned as described by Rezende et al. (2011). As already discussed, in addition to the characteristic signals of raw SB, the NMR spectrum of SBSPy exhibited two particular regions associated with the chemical modification of raw SB with SA and PyA. Region A, from 24 to 40 ppm, was related to the ^{13}C chemical shifts of carbon atoms of methylene groups present in the succinyl unit, while region B, from 120 to 140 ppm, was related to the ^{13}C chemical shifts of carbon atoms of the aromatic ring present in the pyromellityl unit introduced into the SB structure. The area of region B increased as a result of the introduction of pyromellityl units into the SB structure. Other evidence of the chemical modification of raw SB was the increase in the area of signals in the 160–180 ppm region, related to the carbon atoms of the ester carbonyls of acetyl groups, present in hemicelluloses, and of the carboxyls of pyromellityl and succinyl units introduced into the SB structure (Melo et al. 2011). Using the approach presented in the "13C Multiple cross-polarization solid-state nuclear magnetic resonance (13C Multi-CP SS NMR) spectroscopy" section, the numbers of succinyl and pyromellityl units introduced into the SB structure, per cellobiose unit, were 0.71 ± 0.02 and 0.25 ± 0.03, respectively. These results showed that the introduction of both PyA and SA into the SB structure had been successfully accomplished. The proposed structure for SBSPy, based on the results obtained in the present study, is shown in Figure 5b.

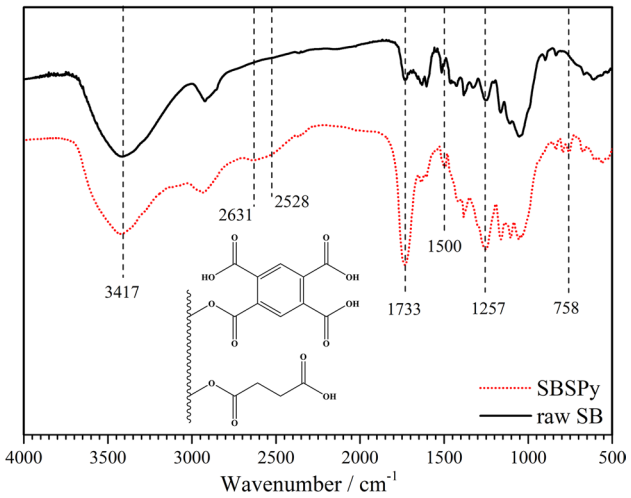

Figure 4 FTIR spectra of raw SB and SBSPy (1% w w^{-1} of raw SB or SBSPy in KBr)

NMR relaxometry

The ^1H NMR relaxometry technique was used to assess the pore structures of raw SB and SBSPy. The T_2 values are directly related to the variation in the sizes of regions filled with a fluid, with longer T_2 values corresponding to larger pores (Mitchell et al. 2005). For lignocellulosic biomass, NMR relaxometry usually reveals different interstitial scales, which are related to different compartments of the microstructure of the plant. T_2 values of a few milliseconds are related to interstitial spaces on the surface of the cellulose microfibril structure, while the intermediate scale, with

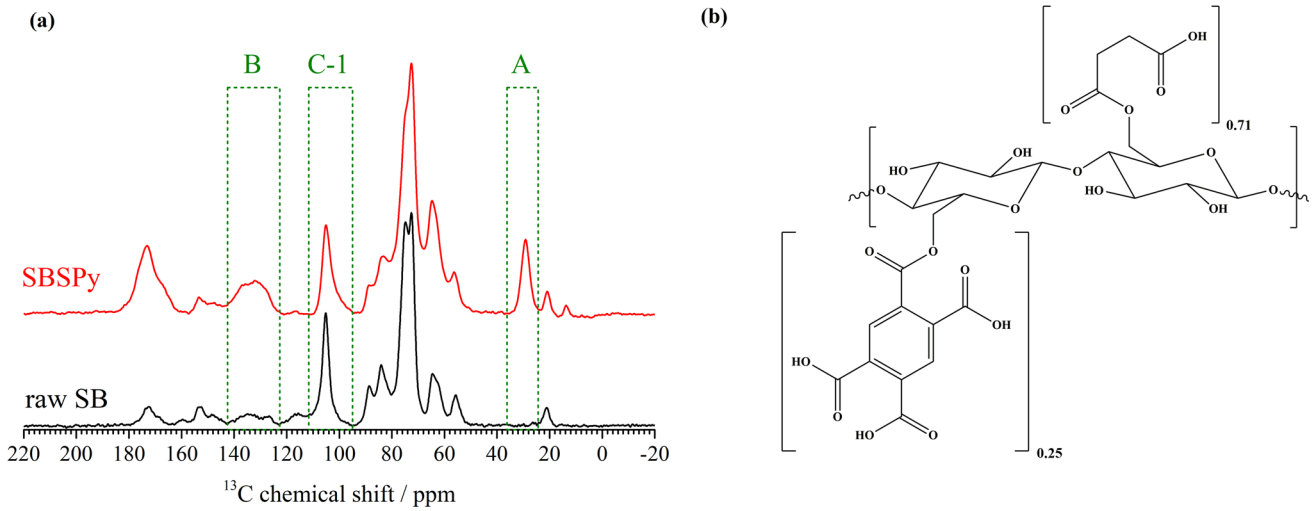

Figure 5 **a** ^{13}C Multi-CP SS NMR spectra of raw SB and SBSPy, and **b** proposed chemical structure for SBSPy based on ^{13}C Multi-CP SS NMR data ($n = 1$ for cellobiose)

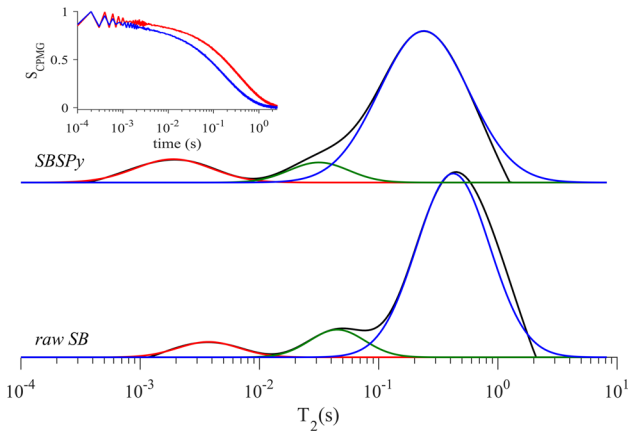

Figure 6 T_2 distributions for raw SB and SBSPy. The black lines indicate the distribution obtained from the ILT procedure. The red, green, and blue components are assigned to the inner microfibril, cell wall, and lumen interstitial spaces, respectively. The inset shows the averages of the CPMG signals for raw SB (red) and SBSPy (blue)

T_2 values of tens of milliseconds, is associated with pores within the lignin-hemicellulose matrix on the surface of the fibers. For T_2 values in the region of hundreds of milliseconds, the related interstitial scale is associated with the luminal pores or spaces between the fibers (Meng & Ragauskas 2014, Tsuchida et al. 2014).

The samples of raw SB and SBSPy were centrifuged to remove any DMA molecules that were not confined within the porous structures of the materials, in order to ensure the reproducibility of the measurements. However, there was no control of the mass and amount of DMA in each measurement, so only the proportions of DMA could be assessed for each interstitial scale. Figure 6 shows the T_2 distributions (normalized by the total area) obtained for raw SB and SBSPy, together with the corresponding deconvolutions. Comparing raw SB with SBSPy, the main difference was the greater access of DMA molecules to the smallest interstitial scale for the SBSPy sample, as shown by the higher relative area (Table 3). This increase was accompanied by reduction of the relative areas for the interstitial scales related to the lignocellulosic matrix (cell wall) and luminal spaces (lumen), a feature that was not observed so clearly for SBSPh and SBST (Almeida et al. 2019, Elias et al. 2019). This could have been a consequence of the differences in the synthesis methods applied for each material.

For all three interstitial scales, the T_2 values for SBSPy were lower than the corresponding values for raw SB (Table 3). This reduction was probably related to changes in the surface relaxivity, since the average pore diameter

Table 3 Central T_2 values and relative areas for each deconvoluted component in the T_2 distributions

Sample	raw SB		SBSPy	
Interstitial scale	Relative area/%	T_2/s	Relative area/%	T_2 s
Microfibril surface	6 ± 1	$(3.7 \pm 0.3) \times 10^{-3}$	11 ± 1	$(1.9 \pm 0.3) \times 10^{-3}$
Lignin-cellulose matrix	10 ± 1	$(4.5 \pm 0.1) \times 10^{-2}$	7 ± 2	$(3.2 \pm 0.2) \times 10^{-2}$
Lumen	85 ± 1	$(4.2 \pm 0.1) \times 10^{-1}$	82 ± 1	$(2.4 \pm 0.1) \times 10^{-1}$

showed almost no difference between the samples, according to the results of the BJH and BET analyses, while the maximum pore size, here associated with the cell wall pores, decreased by 74%. This effect was more pronounced for the inner microfibril and lumen scales, with the central T_2 values decreasing by 49% and 43%, respectively, while the T_2 value for the cell wall decreased by 29%. The results indicated that introduction of the succinyl and pyromellityl units changed the surface of the pores, since the surface relaxivity effects were observed to a lesser extent for SBSPh and SBST (Almeida et al. 2019, Elias et al. 2019).

Scanning electron microscopy

Figure 7 shows SEM micrographs of raw SB (a, c, and e) and SBSPy (b, d, and f) at 60 × (a and b), 500 × (c and d),

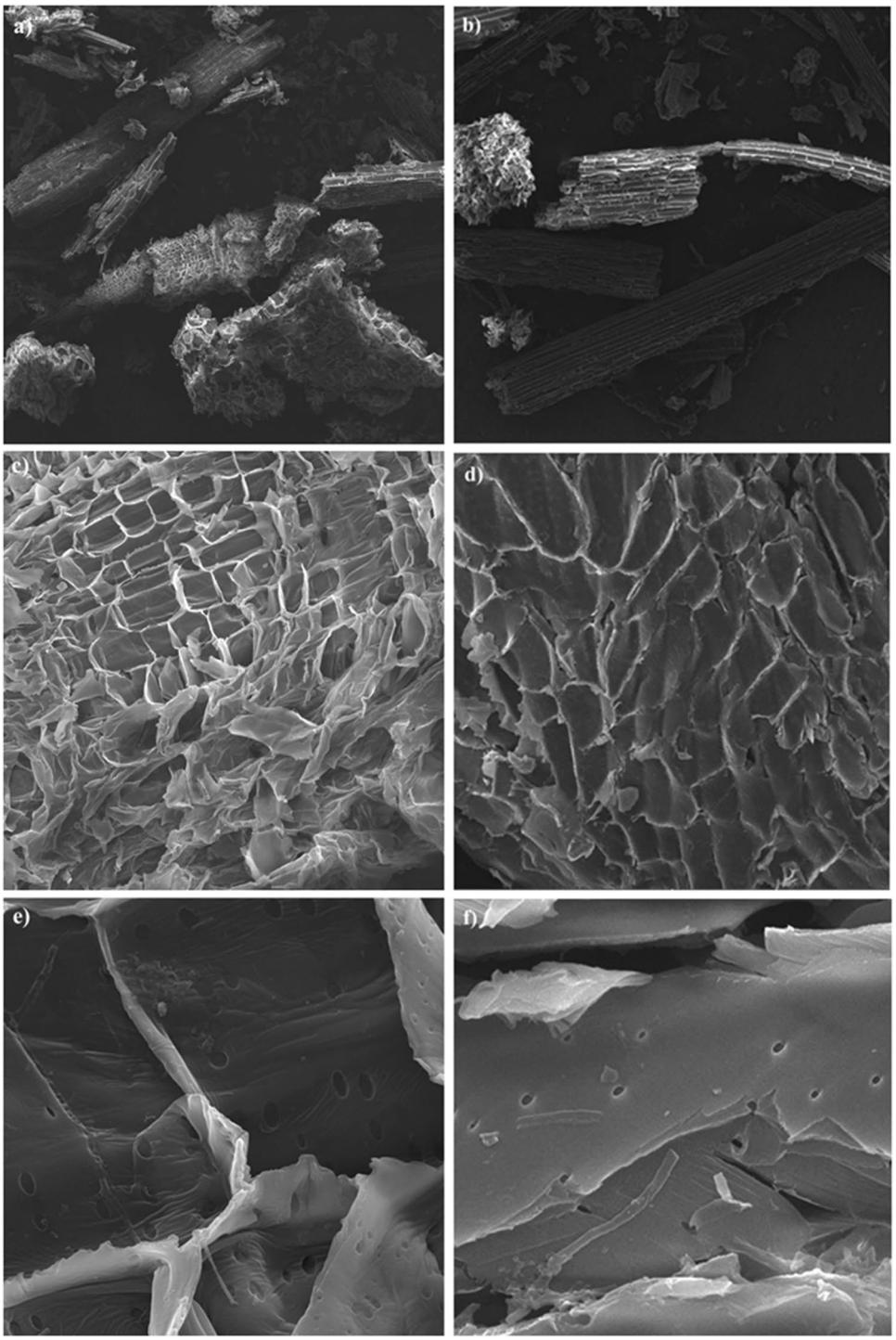

Figure 7 SEM micrographs of raw SB (**a**, **c**, and **e**) and SBSPy (**b**, **d**, and **f**) at 60 × (**a** and **b**), 500 × (**c** and **d**), and 5000 × (**e** and **f**) magnifications

and 5000 × (e and f) magnifications. During the milling process, using a Wiley mill, the tangential shear forces led to partial disintegration of the SB fibers, producing elements with different sizes and shapes (Figure 7a). As expected, the SEM micrographs (Figure 7a–e) did not reveal significant morphological differences between raw SB and SBSPy. This showed that the chemical modification of raw SB with SA and PyA did not significantly change the plant cell structure, as also indicated by NMR relaxometry. This was an important result, since preservation of the plant cell structure, together with the rigidity of the cellulose fibers and their aggregation with the other cell wall components (hemicelluloses and lignin), was essential for the physical, chemical, and biological stability of the biosorbent material.

Batch adsorption

Effect of solution pH on metal ion removal

The solution pH strongly affected the SBSPy adsorption capacities (q_e) for Cu(II) and Zn(II) (Figure 8). Since the pH_{PZC} of SBSPy was 3.11 (see Figure S7 in the Online Resources), the adsorption of both metal ions was favored at pH > pH_{PZC}, at which deprotonation of the carboxylic acid groups resulted in the surface of SBSPy becoming negative. The q_e for Cu(II) and Zn(II) adsorption on SBSPy increased as the solution pH increased, with the highest q_e value reached at pH 5.5, for both metal ions. In contrast, at pH < pH_{PZC}, the carboxylic acid groups on the surface of SBSPy were protonated, so there was no adsorption of either of the metal ions. Therefore, pH 5.5 was selected in the subsequent Cu(II) and Zn(II) adsorption studies. Adsorption of the metal ions at pH higher than 5.5 was not considered, in order to avoid the formation of hydrolyzed species such as $M(OH)^+$ and $M(OH)_2$ (M = Cu or Zn).

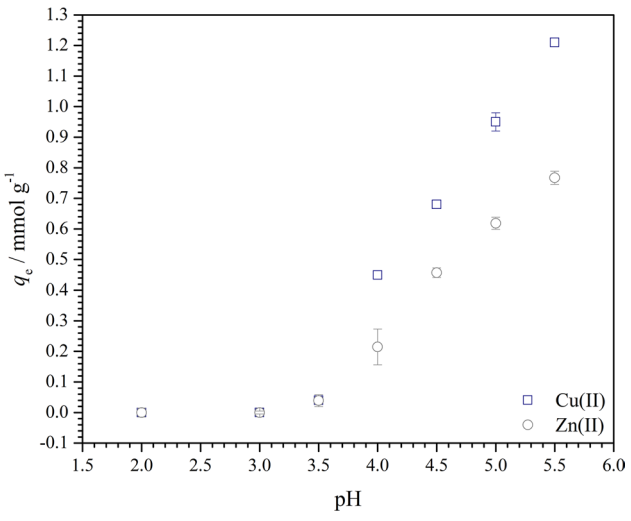

Figure 8 Effect of solution pH on the adsorption capacity of SBSPy for Cu(II) and Zn(II) ([Cu(II)] = [Zn(II)] = 0.79 mmol L^{-1}, 130 rpm, 25 °C, 10 h)

Adsorption kinetics

The kinetic parameters were estimated using the IPD, Boyd, and HSDM models applied to the data for adsorption of Cu(II) and Zn(II) on SBSPy as a function of time (Table 4). The IPD plots for adsorption of Cu(II) and Zn(II) on SBSPy can be found in the Online Resources (Figure S8). The IPD plots were multilinear, exhibiting three stages. Each stage was defined based on the method of piecewise linear regression (Malash & El-Khaiary 2010). The first stage was related to film diffusion of metal ions through the boundary water layer surrounding the SBSPy particles (external mass transfer). The second stage was related to intraparticle diffusion of metal ions on the surface and in the pores of the SBSPy particles (surface and pore diffusion), and the third stage was attributed to adsorption equilibrium. Therefore, the adsorption of both metal ions was initially controlled by film diffusion, followed by a change to intraparticle diffusion (Hameed & El-Khaiary 2008). The $k_{d,1}$ values showed that film diffusion of Cu(II) was faster than that of Zn(II), while the $k_{d,2}$ values showed that intraparticle diffusion was similar for Cu(II) and Zn(II). The faster film diffusion of Cu(II) could be explained by its smaller hydrated ionic radius (r_H) ($r_{H,Cu}$ = 4.19Å, $r_{H,Zn}$ = 4.30 Å) (Nightingale 1959). The Boyd plots for Cu(II) and Zn(II) adsorption on SBSPy can be found in the Online Resources (Figure S9). According to Boyd et al. (1947), the plot of B_t against t should produce a straight line that crosses the origin (0,0), when intraparticle diffusion is the rate-limiting step of the adsorption. Hence, the intraparticle diffusion coefficient (D_i) can be determined by the slope (B) of the straight line. However, in the present case, the Boyd plots for both metal ions produced straight lines that did not cross the origin (Table 4). This suggested that intraparticle diffusion was not the only step controlling the overall kinetics for adsorption of Cu(II) and Zn(II) on SBSPy, which was in agreement with the IPD plots.

Figure 9 shows the plots of q_t against t for adsorption of Cu(II) and Zn(II) on SBSPy, together with the curves fitted to the experimental data using the HSDM model. This model was used to describe the adsorption through the particle radius and to estimate the effective diffusion coefficient. The film mass transfer coefficient (k_f) and the surface diffusion coefficient (D_s) were used to determine the Biot number (Bi), which characterizes the ratio of the external and internal mass transfer resistances (Worch 2012). The values of k_f, D_s, and Bi obtained from HSDM model are presented in Table 4. The k_f and D_s values were similar for the two metal ions, with Cu(II) exhibiting slightly lower k_f value and higher D_s value than Zn(II)

Table 4 Results of nonlinear regression (NLR) analysis of the kinetic data ([Cu(II)] = [Zn(II)] = 0.79 mmol L^{-1}), results of NLR analysis of the equilibrium data ([Cu(II)] = [Zn(II)] = 0.03–3.11 mmol L^{-1}), and results of modeling the breakthrough curves for adsorption of Cu(II) and Zn(II) on SBSPy in a fixed-bed column. The kinetic and equilibrium studies in batch mode employed 0.2 g L^{-1} SBSPy, 130 rpm, 25 °C, and pH 5.5. The continuous adsorption studies using a fixed-bed column employed [Cu(II)] = [Zn(II)] = 1.4 mmol L^{-1}, pH 5.5, 25 °C, V = 2.35 mL min^{-1}, Z = 3.0 cm, and 0.5 g SBSPy

Model	Parameter	Cu(II)	Zn(II)
Kinetics			
Experimental data	C_i/mmol L^{-1}	0.79	0.79
	t_e/min	120	180
Intraparticle diffusion (IPD)	*1st stage*		
	$k_{d,1}$/mmol g^{-1} $min^{-1/2}$	0.12 ± 0.01	0.06 ± 0.02
	C/mmol g^{-1}	0.26 ± 0.03	0.105 ± 0.008
	R^2	0.9804	0.9884
	R^2_{adj}	0.9739	0.9825
	2nd stage		
	$k_{d,2}$/mmol g^{-1} $min^{-1/2}$	0.020 ± 0.002	0.021 ± 0.003
	C/mmol g^{-1}	0.72 ± 0.03	0.48 ± 0.02
	R^2	0.9196	0.9212
	R^2_{adj}	0.9035	0.9015
Boyd plot	B (slope)	0.0344	0.0356
	B_t (intercept)	0.1559	0.0247
HSDM	k_F/m s^{-1}	1.18×10^{-5}	1.41×10^{-5}
	D_s/m^2 s^{-1}	9.00×10^{-14}	8.53×10^{-14}
	R^2	0.9508	0.9690
	R^2_{adj}	0.9321	0.9512
	χ^2_{red}	0.0035	0.0021
	Bi (Biot number)	17.8	25.3
Equilibrium			
Experimental data	$Q_{max,exp}$/mmol g^{-1}	1.19 ± 0.05	0.95 ± 0.02
	I_e/mol L^{-1}	0.6119	0.6074
	γ_e	0.236	0.236
Langmuir	Q_{max}/mmol g^{-1}	1.21 ± 0.05	1.01 ± 0.01
	b/L $mmol^{-1}$	18 ± 3	5.2 ± 0.4
	R^2	0.9514	0.9979
	R^2_{adj}	0.9482	0.9977
	χ^2_{red}	0.0127	0.0005
Sips	Q_{max}/mmol g^{-1}	1.4 ± 0.1	1.05 ± 0.02
	b/L $mmol^{-1}$	12 ± 4	4.5 ± 0.2
	n	1.6 ± 0.2	1.08 ± 0.03
	R^2	0.9761	0.9988
	R^2_{adj}	0.9727	0.9986
	χ^2_{red}	0.0069	0.0003
Fixed-bed column			
Experimental data	$Q_{max,exp}$/mmol g^{-1}	0.92 ± 0.06	0.810 ±0.08
	ε_{exp}	0.5	0.5
	t_b/min	65	46
	t_e/min	300	280
	H/cm	1.42	1.13
	EAP/%	83.7	74.6
	Z_{MTZ}/cm	2.35	2.51
Thomas	k_{Th}/mL min^{-1} $mmol^{-1}$	19.65	20.94
	Q_{max}/mmol g^{-1}	0.891 ± 0.005	0.793 ± 0.003
	$RMSE$	0.066	0.058
	R^2	0.972	0.975
	R^2_{adj}	0.967	0.970
	χ^2_{red}	0.012	0.012

Table 4 (continued)

Model	Parameter	Cu(II)	Zn(II)
Bohart-Adams	$k_{B\text{-}A}$/mL min^{-1} mmol^{-1}	19.69	19.50
	Q_{max}/mmol g^{-1}	0.893 ± 0.007	0.781 ± 0.002
	RMSE	0.056	0.065
	R^2	0.980	0.970
	R^2_{adj}	0.976	0.965
	χ^2_{red}	0.010	0.013
ILE-Langmuir	D_L/mm^2 min^{-1}	1.11×10^{-4}	1.20×10^{-4}
	RMSE	18	17
	R^2	0.933	0.950
	χ^2_{red}	3.24	2.91

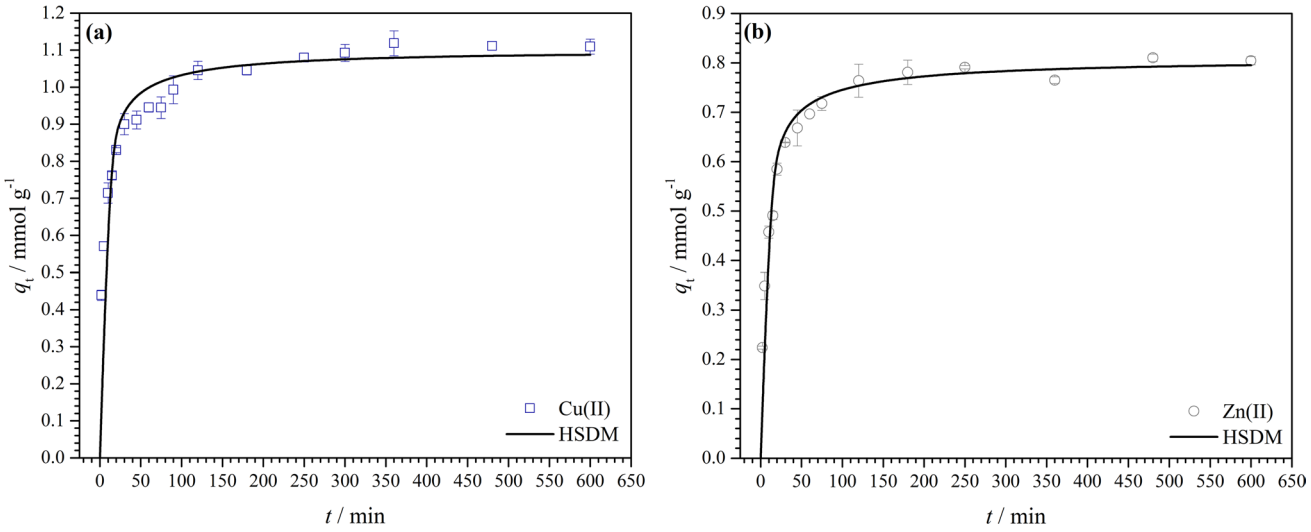

Figure 9 Plot of q_t against t for adsorption of **a** Cu(II) and **b** Zn(II) on SBSPy ([Cu(II)] = [Zn(II)] = 0.79 mmol L^{-1}, 0.2 g L^{-1} SBSPy, 130 rpm, 25 °C, pH 5.5)

(Table 4). If $Bi > 100$, the overall kinetics is controlled by surface diffusion (intraparticle mass transfer), while if $Bi < 1$, film diffusion (external mass transfer) controls the overall kinetics. If $1 < Bi < 100$, both diffusions are relevant for the overall kinetics (Guibal et al. 1998, Prasad & Srivastava 2009). Therefore, a lower *Bi* value is associated with greater film diffusion, relative to intraparticle diffusion (Worch 2012). Since the *Bi* values were higher than 1 ($Bi_{Cu} = 17.8$ and $Bi_{Zn} = 25.3$), but much lower than 100, both external and internal diffusion contributed to the overall kinetics, as suggested by the IPD model. Plots of the adsorption capacities (q_t) for Cu(II) and Zn(II) on SBSPy, as a function of time and the radial coordinate (r), are shown in Figure 10. Both metal ions were adsorbed at higher r values, because the adsorption initially occurred at the outer surface of the SBSPy particles ($r = R$), with a few minutes being required for adsorption to occur in the pores of the particles. This was in agreement with the first and second steps of the IPD model, as well as with the *Bi* values obtained.

Adsorption isotherms

The effects of the initial metal ion solution concentrations on the q_e values for adsorption of Cu(II) and Zn(II) on SBSPy are shown in Figure 11, together with the curves fitted to the adsorption data using the Langmuir and Sips models. The estimated isotherm parameters are shown in Table 4. Both isotherm models were able to describe the adsorption of Cu(II) and Zn(II) on SBSPy. The Sips model is a three-parameter model, so it can provide better fits to adsorption data, compared to the two-parameter Langmuir model. However, despite showing slightly lower R^2_{adj} values and higher χ^2_{red} values, the maximum adsorption

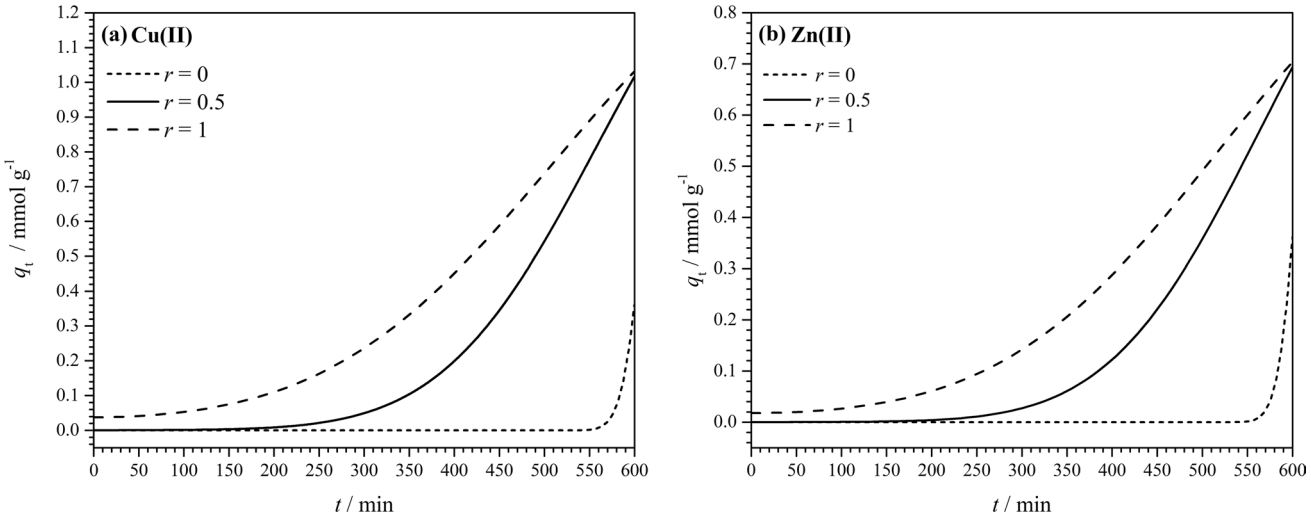

Figure 10 Adsorption capacity (q_t) for **a** Cu(II) and **b** Zn(II), as a function of time and the radial coordinate (r)

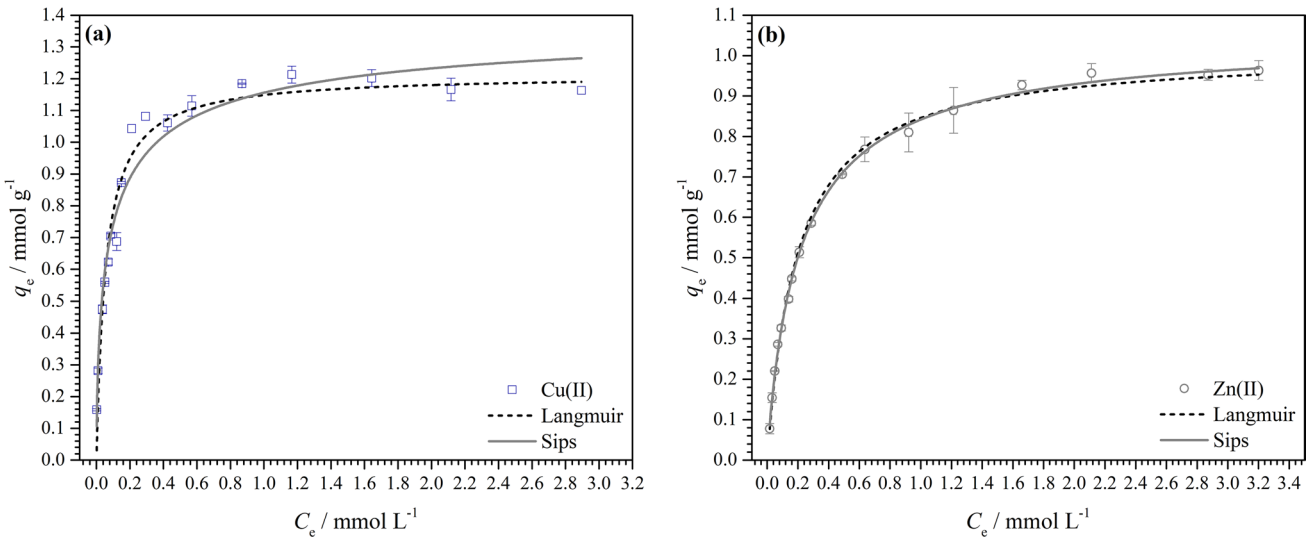

Figure 11 Isotherms for adsorption of **a** Cu(II) and **b** Zn(II) on SBSPy ([Cu(II)] = [Zn(II)] = 0.033–3.11 mmol L^{-1}, 0.2 g L^{-1} SBSPy, pH 5.5, $t_{Cu(II)}$ = 120 min, $t_{Zn(II)}$ = 180 min, 25 °C)

capacities (Q_{max}) predicted by the Langmuir model were closer to the experimental Q_{max} values. The parameter n of the Sips model is related to the heterogeneity of the system under study (Do 1998). A value of n different from unity indicates that the adsorption system diverges from the homogeneity assumed by the Langmuir model. The Langmuir constant (b) is associated with the adsorbate-adsorbent affinity, such that the higher the b value, the greater the affinity of the metal ion for the adsorption site. Since $b_{Cu(II)} > b_{Zn(II)}$, the affinity of the Cu(II) ions for the SBSPy adsorption sites was greater than the affinity of the Zn(II) ions for the sites. This was in agreement with the results reported by Bunting and Thong (1970), who investigated the relative stabilities of complexes formed between various divalent metal ions and carboxylate anions.

Regeneration and reuse of SBSPy

The feasibility of regeneration and reuse of the SBSPy was evaluated in an adsorption-desorption-(re)adsorption cycle. The SBSPy showed E_{des} of 88.8 ± 0.6% and $E_{re\text{-}ads}$ of 94 ± 2% for Cu(II), and E_{des} of 99 ± 1% and $E_{re\text{-}ads}$ of

95 ± 2% for Zn(II). Xavier et al. (2018) demonstrated that continuous desorption in a fixed-bed column of raw SB modified with TA was able to remove metal ions (Co(II), Cu(II), and Ni(II)) not desorbed in previous cycles, because the higher concentration gradient between the non-desorbed metal ions on the adsorbent surface and the inlet desorption solution provided a higher driving force for desorption.

Evaluation of adsorption thermodynamics

Changes in enthalpy of adsorption ($\Delta_{ads}H$)

A plot of $\Delta_{ads}H$ against SBSPy surface coverage (θ) is shown in Figure 12. The $\Delta_{ads}H$ values indicated that for both metal ions, adsorption on the SBSPy surface was an endothermic process. At $\theta < 0.3$, the curves exhibited different behaviors, with the Zn(II) adsorption process becoming less endothermic, which was opposite to the behavior observed for the Cu(II) adsorption process. At $\theta = 0.3$, the $\Delta_{ads}H$ values were the same for adsorption of the two metal ions, suggesting that at this surface coverage, the balance of intermolecular interactions was similar for the two adsorption systems. At $\theta > 0.3$, the curves for the SBSPy-Cu(II) and SBSPy-Zn(II) systems exhibited similar trends, with the $\Delta_{ads}H$ values becoming less endothermic as SBSPy surface coverage increased. However, the $\Delta_{ads}H$ values for the SBSPy-Zn(II) system became less endothermic than for the SBSPy-Cu(II) system, suggesting that different subprocesses were involved in the adsorption of Cu(II) and Zn(II) on SBSPy.

The $\Delta_{ads}H$ value (Figure 12) was the result of the contributions of three subprocesses (Eq. (12)) that occurred during adsorption of the metal ions on SBSPy, as follows:

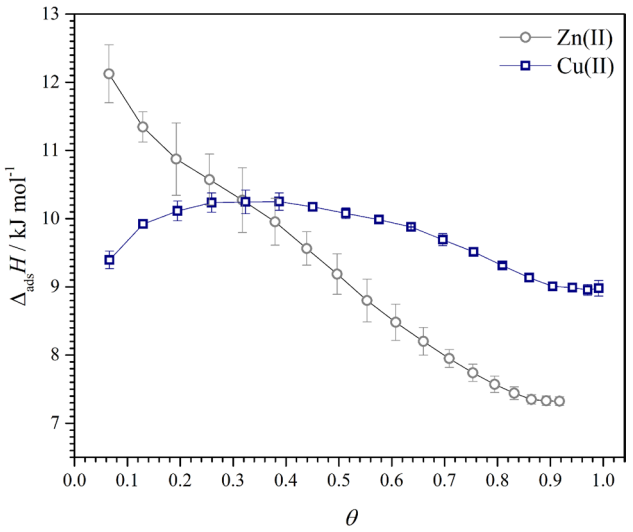

Figure 12 Changes in enthalpy of adsorption of Cu(II) and Zn(II), as a function of SBSPy surface coverage (θ) (pH 5.5, 25 °C)

$$\Delta_{ads}H = \Delta_{desol}H^{SBSPysite,metal} + \Delta_{int}H^{metal-metal} + \Delta_{int}H^{SBSPysite-metal} \quad (12)$$

where $\Delta_{desol}H^{SBSPy\ site,\ metal}$ is the change in enthalpy due to the desolvation of metal ions and SBSPy adsorption sites, $\Delta_{int}H^{metal\text{-}metal}$ is the change in enthalpy due to the metal-metal interaction, and $\Delta_{int}H^{SBSPy\ site\text{-}metal}$ is the change in enthalpy due to the formation of interactions between the metal ions and the SBSPy adsorption sites (Teodoro et al. 2016).

The $\Delta_{desol}H^{SBSPy\ site,\ metal}$ subprocess was endothermic, since desolvation of the SBSPy adsorption sites and metal ions required energy. The $\Delta_{int}H^{metal\text{-}metal}$ subprocess could be endothermic, if metal ion-metal ion interactions in solution were disrupted and/or repulsion occurred between adsorbed species on the surface of SBSPy, or exothermic, if metal ion-metal ion interactions occurred in solution and/or on the surface of SBSPy. The $\Delta_{int}H^{SBSPy\ site\text{-}metal}$ subprocess was exothermic, because the formation of interactions between two oppositely charged species releases energy (Marcus 1994, McMurray & Fay 2004).

As discussed previously, it was expected that Zn(II) ions, which are slightly softer than Cu(II) ions, would have more affinity for the carboxylate groups of pyromellitate units, while Cu(II) ions would have more affinity for the carboxylate groups of succinate units. In addition, the affinity of the SBSPy adsorption sites for Cu(II) ions ($b_{Cu(II)}$ = 18 L mmol^{-1}) was greater than for Zn(II) ions ($b_{Zn(II)}$ = 5.2 L mmol^{-1}). Therefore, a possible explanation for the different behaviors of the curves of $\Delta_{ads}H$ as a function of θ, for adsorption of Cu(II) and Zn(II) on SBSPy, was the formation of complexes with different stabilities between the SBSPy adsorption sites and the metal ions, resulting in different $\Delta_{int}H^{SBSPy\ site\text{-}metal}$ values. At low θ values, the quantity of adsorbed metal ions on the surface of SBSPy was low, so the contribution of $\Delta_{int}H^{metal\text{-}metal}$ could be neglected. However, the $\Delta_{int}H^{metal\text{-}metal}$ value probably became significant with increasing coverage of the SBSPy surface by metal ions, because the distances between the positively charged adsorbed species decreased.

For the SBSPy-Zn(II) system, $\Delta_{ads}H$ decreased with increasing θ, in the entire θ range studied. The same behavior was not observed for the SBSPy-Cu(II) system, where $\Delta_{ads}H$ only decreased at $\theta > 0.3$. For the SBSPy-Cu(II) system, $\Delta_{ads}H$ increased until θ reached 0.3, indicating that endothermic contributions ($\Delta_{desol}H^{SBSPy\ sites,\ metal}$ and $\Delta_{int}H^{metal\text{-}metal}$) probably dominated the adsorption enthalpy balance. Since the $\Delta_{desol}H^{SBSPy\ sites,\ metal}$ values changed slightly during the global adsorption process, due to energy differences of the different adsorption sites, the different contributions of $\Delta_{int}H^{SBSPy\ site\text{-}metal}$ and $\Delta_{int}H^{metal\text{-}metal}$ determined the $\Delta_{ads}H$ value. The differences in $\Delta_{int}H^{SBSPy\ site\text{-}metal}$ during Cu(II) and Zn(II) adsorption on SBSPy were mainly related to the

presence of different adsorption sites on SBSPy, with different affinities for Cu(II) and Zn(II), namely, the carboxylate groups of succinyl (0.71) and pyromellityl (0.25) units. On the other hand, the differences in $\Delta_{int}H^{metal\text{-}metal}$ during the adsorption of Cu(II) and Zn(II) on SBSPy were mainly related to different interactions between metal ion species adsorbed on the surface of SBSPy, as the θ value increased. Therefore, the less positive $\Delta_{ads}H$ values for Zn(II) adsorption, compared to Cu(II) adsorption, could be mainly attributed to different balances between $\Delta_{int}H^{SBSPy\ site\text{-}metal}$ and $\Delta_{int}H^{metal\text{-}metal}$, in the θ range studied.

Changes in free energy and adsorption entropy

The thermodynamic parameters for adsorption of Cu(II) and Zn(II), respectively, on SBSPy were $\Delta_{ads}G° = -28 \pm 1$ and -25 ± 1 kJ mol^{-1}, $\Delta_{ads}H° = 9.3 \pm 0.2$ and 14.2 ± 0.1 kJ mol^{-1}, and $T\Delta_{ads}S° = 37 \pm 1$ and 39 ± 1 kJ mol^{-1}. For thermodynamic processes at constant temperature and pressure, $\Delta_{ads}G$ is the thermodynamic potential of the process. Teodoro et al. (2016), Elias et al. (2019), and Almeida et al. (2019) reported similar adsorption energy changes for transition metals (Co(II), Cu(II), and Ni(II)) adsorbed on cellulosic and lignocellulosic materials modified with different carboxylic acid anhydrides. For both systems studied here, the $\Delta_{ads}G°$ values were negative, with the migration of metal ions from the liquid phase to the SBSPy surface prevailing over the free forms of adsorbent and adsorbate in solution. The $\Delta_{ads}H°$ and $T\Delta_{ads}S°$ values were positive for the two systems studied here, indicating that the adsorption of both metal ions on the surface of SBSPy was entropically favored. The entropic contribution could be mainly attributed to water molecules released from the solvation shells of metal ions and the SBSPy adsorption sites, and the corresponding balance associated with migration of the metal ions from the bulk solution to the surface of SBSPy, to form new interactions. The magnitude of the $T\Delta_{ads}S°$ term for adsorption of both metal ions on SBSPy suggested that water molecules from the solvation shells of the metal ions migrated to the solution after adsorption, which could be attributed to the formation of inner-sphere complexes between SBSPy adsorption sites and metal ions. Since the $\Delta_{ads}H$ values obtained by ITC included the contributions of three subprocesses, including $\Delta_{int}H^{SBSPy\ site\text{-}metal}$, it was not possible to use the $\Delta_{ads}H$ value to distinguish between physisorption and chemisorption.

Continuous adsorption in a fixed-bed column

The amounts of adsorbed (w_{ads}) and desorbed (w_{des}) metal ions, the maximum adsorption capacity of the bed ($Q_{max,exp}$), and the desorption efficiency (E_{des}) for each cycle are shown in Table 5 for the two adsorption systems studied. The regeneration of SBSPy proved to be feasible, since the E_{des} values were close to 100% in all the cycles. The values of the operating parameters (Table 5) for the adsorption cycles indicated that there were no significant decreases of $Q_{max,exp}$ for the two adsorption systems. Therefore, it was feasible to use SBSPy as an adsorbent in several cycles. These results showed the technical viability of using SBSPy as an adsorbent in a fixed-bed column to remove metal ions from contaminated water.

Table 5 Operating parameters used in three cycles of adsorption and desorption of Cu(II) and Zn(II) on SBSPy in a fixed-bed column at 25 °C

Metal ion	Parameter	Cycle number		
		1st	2nd	3rd
Cu(II)	w_{ads}/mmol	0.463	0.459	0.455
	w_{des}/mmol	0.462	0.458	0.454
	$Q_{max,exp}$/mmol g^{-1}	0.926	0.919	0.915
	E_{des}/ %	99.8	99.9	99.9
Zn(II)	w_{ads}/mmol	0.405	0.392	0.402
	w_{des}/mmol	0.403	0.390	0.400
	$Q_{max,exp}$/mmol g^{-1}	0.810	0.784	0.804
	E_{des}/%	99.7	99.4	99.4

The curves obtained by fitting of the experimental data using the Thomas, Bohart-Adams, and ILE models are shown in Figure 13. The estimated model parameters obtained by the fitting are provided in Table 4. For both adsorption systems, the Thomas and Bohart-Adams provided satisfactory fits to the experimental data, with low *RMSE* and χ^2_{red} values, and high R^2_{adj} values. In addition, the Q_{max} values estimated by the Thomas and Bohart-Adams were close to the $Q_{max,exp}$ values. According to Chu (2010), when $bC_0 >> 1$, the Langmuir isotherm approaches the rectangular isotherm and, consequently, the Thomas model approximates to the Bohart-Adams model, with the pseudo-second-order rate constant (k_{Th}) of the Thomas model approximating to the quasi-chemical rate constant ($k_{B\text{-}A}$) of the Bohart-Adams model. Therefore, since $bC_0 >> 1$ for both adsorption systems studied (25.2 with Cu(II) and 7.3 with Zn(II)), the Thomas and Bohart-Adams models could be used to describe the adsorption of both metal ions on SBSPy. The adsorption rate constants, k_{Th} and $k_{B\text{-}A}$, consider the combination of all the steps involved in the adsorption process (film diffusion, intraparticle diffusion, and adsorption). For the two adsorption systems studied, the k_{Th} and $k_{B\text{-}A}$ values were similar, under the same operating conditions.

The ILE model was also used to model the breakthrough curve and estimate the operating parameters of the continuous adsorption system. In order to fit the breakthrough curve, this model is fed with the physical properties of the adsorbent and the adsorption parameters obtained from

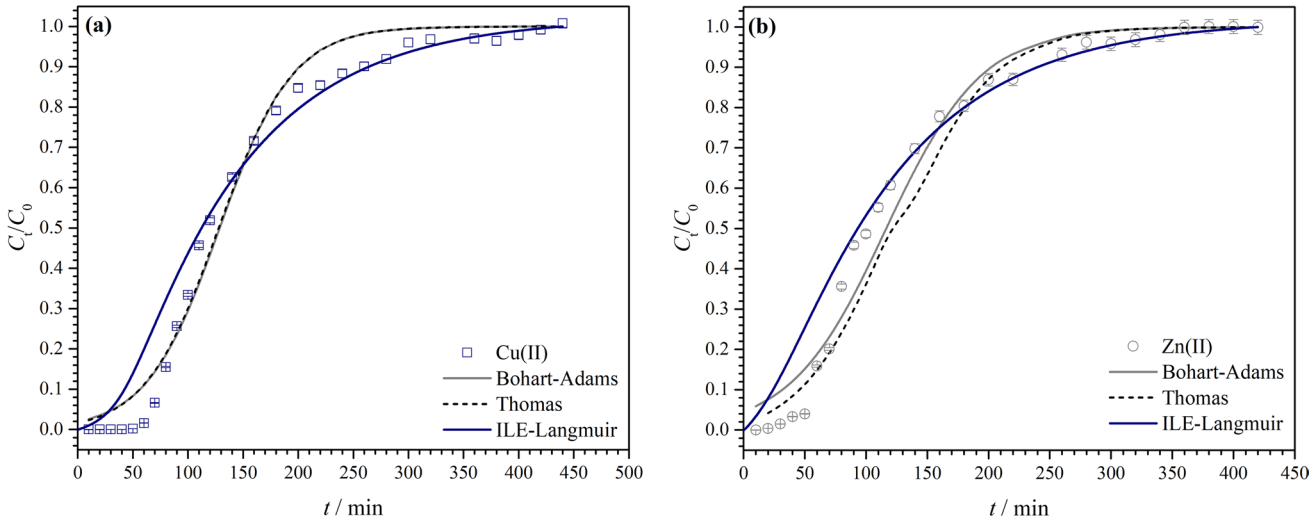

Figure 13 Breakthrough curves for adsorption of **a** Cu(II) and **b** Zn(II) on SBSPy in a fixed-bed column at 25 °C ([Cu(II)] = [Zn(II)] = 1.4 mmol L^{-1}, pH 5.5, $V = 2.35$ mL min^{-1}, 0.5 g SBSPy)

single batch adsorption. To solve the ILE model, the Langmuir isotherm was used, since it provided the best description of single batch adsorption of Cu(II) and Zn(II) on SBSPy. As shown in Figure 13a–b, the ILE-Langmuir model provided a good fit to the breakthrough curve, especially for the experimental data closer to bed saturation, but with poorer prediction of the initial data points closer to the breakthrough point. This could have been related to the assumptions of the model, which uses an approximation by local and instantaneous equilibrium, assuming that the mass transfer of the solute from the fluid to the solid is relatively fast, with axial dispersion being considered relevant for the process.

The mass transfer resistance for transport of the solute from the fluid to the solid was high, as shown by the steepness of the breakthrough curve, which is directly proportional to the mass transfer resistance (Worch 2012). This high mass transfer resistance could provide an explanation for the lower Q_{max} values obtained for continuous adsorption in a fixed-bed column, compared to single batch adsorption. Furthermore, the mass transfer resistance for transport from the fluid to the solid phase is higher in continuous adsorption using a fixed-bed column under a non-turbulent flow regime, compared to batch adsorption (Viegas et al. 2014). Therefore, the use of an inlet flow rate different from that employed here could allow a longer contact time between metal ions in the fluid phase and SBSPy particles, resulting in higher values of Q_{max}, EAP, and H (Xavier et al. 2018). The high inlet flow rate employed in this study also affected the length of the mass transfer zone (Z_{MTZ}), as well as the EAP and H values for both adsorption systems, leading to lower performance than expected in the continuous adsorption operation (Table 4). The EAP and H values for Cu(II) adsorption in a fixed-bed column were higher than for Zn(II) adsorption. Furthermore, the Z_{MTZ} value was higher for Cu(II) adsorption, compared to Zn(II) adsorption. Therefore, this indicated that the mass transfer resistance was lower for Cu(II) adsorption than for Zn(II) adsorption, which was corroborated by the higher steepness of the breakthrough curve for Cu(II) adsorption.

Comparison with literature data for Cu(II) and Zn(II) adsorption on different adsorbent materials

Table 6 lists some adsorbents prepared from cellulose, lignocellulosic biomass, algae, fungal biomass, and vermiculite, used to remove Cu(II) and Zn(II) from single-component spiked aqueous solutions, employing batch and fixed-bed column systems, in the pH range from 2 to 6.3. For batch adsorption, SBSPy at low adsorbent dosage exhibited high Q_{max} values for Cu(II) and Zn(II), which were comparable to the values reported in the literature. The Q_{max} values of SBSPy for Cu(II) and Zn(II) were much higher than the values obtained using raw SB. For continuous adsorption in a fixed-bed column, SBSPy also exhibited high Q_{max} values for Cu(II) and Zn(II). In addition, the ability to regenerate and reuse SBSPy in both batch and continuous modes confirmed its potential as an adsorbent for metal ions, since it could enable not only the removal of pollutants from an effluent, but also the recovery of the metal ions for possible reuse.

Conclusions

The chemical modification of raw SB with succinic and pyromellitic anhydrides, using a one-pot reaction, was successfully accomplished, yielding an efficient, selective, and

Table 6 Compilation of different adsorbent materials reported in the literature for removal of Cu(II) and Zn(II) from single-component spiked aqueous solutions in batch and continuous (fixed-bed column) systems

Type of biomass	Modifying agent	Q_{max}/mmol g^{-1}		pH	Adsorbent dosage/g L^{-1}	Agitation speed/rpm	*T*/°C	Reference
		Cu(II)	Zn(II)					
Sugarcane bagasse	PA	0.845	-	5.75	0.20	130	25.0	Ramos et al. (2016)
Sugarcane bagasse	TA	1.121	-	5.75	0.20	130	25.0	Ramos et al. (2015)
Cellulose	TA	1.487	-	5.50	0.20	130	25.0	Teodoro et al. (2016)
Mercerized cellulose	SA	2.421		5.4	1.00	-	25.0	Gurgel et al. (2008)
Sugarcane bagasse	PA	1.21	1.00	5.0	0.25	150	Room temperature	Yu et al. (2015)
Sugarcane bagasse	SA and PyA	1.19	0.95	5.75	0.20	130	25.0	This study
Raw sugarcane bagasse	-	0.102	0.015	5.75	0.20	130	25.0	This study
Orange peel	KCl	0.94	0.75	5.0-5.5	5.00	120	25.0	Guo et al. (2011)
Borassus flabellifer/Aspergillus tamari	H_2SO_4	-	0.86	6.0	2.50	-	30.0	Saravanan et al. (2020)
Borassus flabellifer/Aspergillus tamari	-	-	0.76	6.0	2.50	-	30.0	Saravanan et al. (2020)
Type of biomass	**Modifying agent**	**Q_{max}/mmol g^{-1}**		**pH**	**Column height /cm**	**Flow rate/ mL min^{-1}**	***T*/°C**	**Reference**
		Cu(II)	**Zn(II)**					
Neem bark	H_2SO_4	0.525	0.504	2	-	10	-	Maheshwari and Gupta (2016)
Chestnut shell	formaldehyde	0.100	0.084	4.8[a] and 6[b]	15	6	20	Vázquez et al. (2009)
Red seaweeds	-	0.110	0.010	6.3	20.5	10	25	Cechinel et al. (2018)
Wine processing waste sludge	-	0.124	0.092	5	25	10	25	Liu et al. (2011)
Expanded vermiculite	-	0.605	0.540	4.5	15	5	-	Freitas et al. (2017)
Tea waste, maple leaves, and mandarin peel	-	0.997	0.539	5.5	31	10	Room temperature	Abdolali et al. (2017)
Brown algae *Sargassum* sp.	-	1.656	-	4.5	30.6	4	30	Barquilha et al. (2019)
Pongamia (*Pongamia pinnata*) oil cake	-	-	1.014	4.45	14.82	5.59	30	Shanmugaprakash et al. (2018)
Sugarcane bagasse	SA and PyA	0.92	0.81	5.5	3.0	2.35	25	This study

[a]Cu(II), [b]Zn(II)

reusable adsorbent (SBSPy) possessing adsorption sites with different affinities for Cu(II) and Zn(II). The FTIR and ^{13}C Multi-CP SS NMR spectra of SBSPy showed that the order of addition of the carboxylic acid anhydrides directly affected the synthesis yield and, especially, the quantities of succinyl and pyromellityl units introduced into the SB structure. Succinic anhydride should be added to the reaction medium first, in order to introduce more succinyl units

into the SB structure. The results indicated selectivity of the adsorption sites, with the succinate moiety being responsible for increasing Cu(II) adsorption, while the pyromellitate moiety was responsible for increasing Zn(II) adsorption. Analyses using ^{13}C Multi-CP SS NMR showed that under the optimized synthesis condition, 0.25 pyromellityl units and 0.71 succinyl units were covalently linked to each cellobiose unit. Relaxometry analyses showed that interstitial scale spaces decreased. This indicated that the succinyl and pyromellityl groups occupied previously free spaces, mainly at the inner microfibril and lumen scales. The use of diffusion kinetics models indicated that both film and intraparticle diffusion contributed to the adsorption rate. Thermodynamic data showed that the adsorption was endothermic and entropy-driven. SBSPy was successfully used in a fixed-bed column, in three cycles of adsorption-desorption. Therefore, SBSPy has potential to be used as a biodegradable adsorbent in water and wastewater treatment plants, with the advantage of being able to be regenerated and reused, enabling the safe recovery of toxic metal ions removed from contaminated water.

Supplementary Information The online version contains supplementary material available at https://doi.org/10.1007/s11356-021-17549-5.

Acknowledgments The authors are grateful to Dr. Amália L. P. Xavier for her contributions to the methodology and the modeling of the continuous adsorption data. The authors are grateful to Fundação de Amparo à Pesquisa do Estado de Minas Gerais (FAPEMIG, grant number CEX-APQ-01287-15) and Universidade Federal de Ouro Preto (UFOP, grant numbers 23109.000928/2020-33 and 23109.000929/2020-88) for funding this research. L.V.A.G. is also grateful to Conselho Nacional de Desenvolvimento Científico e Tecnológico (CNPq, grant number 307445/2019-4) for the provision of a PQ-2 fellowship. O.F.H.A. is also grateful to Conselho Nacional de Desenvolvimento Científico e Tecnológico (CNPq, grant number 152180/2019-2) for the provision of a PDJ fellowship.

Author contribution Filipe Simões Teodoro: Investigation, methodology, formal analysis, validation, conceptualization, writing—original draft. Liliane Catone Soares: Conceptualization, validation, visualization, writing—review and editing. Jefferson Gonçalves Filgueiras: Investigation, methodology, formal analysis. Eduardo Ribeiro de Azevedo: Investigation, methodology, formal analysis. Álvaro Javier Patino Agudelo: Investigation. Oscar Fernando Herrera Adarme: Investigation, methodology, formal analysis. Luis Henrique Mendes da Silva: Resources. Leandro Vinícius Alves Gurgel: Methodology, formal analysis, validation, conceptualization, visualization, writing (review and editing), project administration, resources, supervision, funding acquisition.

Funding This study was financed in part by Coordenação de Aperfeiçoamento de Pessoal de Nível Superior − Brasil (CAPES, Finance Code 001).

Declarations

Ethical approval and consent to participate Not applicable.

Consent for publication Not applicable.

Competing interests The authors declare no known competing interests.

References

Abdolali A, Ngo HH, Guo W, Zhou JL, Zhang J, Liang S, Chang SW, Nguyen DD, Liu Y (2017) Application of a breakthrough biosorbent for removing heavy metals from synthetic and real wastewaters in a lab-scale continuous fixed-bed column. Bioresour. Technol. 229:78–87. https://doi.org/10.1016/j.biortech.2017.01.016

Almeida FTR, Ferreira BCS, Moreira ALdSL, de Freitas RP, Gil LF, Gurgel LVA (2016) Application of a new bifunctionalized chitosan derivative with zwitterionic characteristics for the adsorption of Cu^{2+}, Co^{2+}, Ni^{2+}, and oxyanions of Cr^{6+} from aqueous solutions: kinetic and equilibrium aspects. J. Colloid Interface Sci. 466:297–309. https://doi.org/10.1016/j.jcis.2015.12.037

Almeida FTR, Elias MMC, Xavier ALP, Ferreira GMD, Silva IA, Filgueiras JG, de Azevedo ER, da Silva LHM, Gil LF, Gurgel LVA (2019) Synthesis and application of sugarcane bagasse cellulose mixed esters. Part II: Removal of Co^{2+} and Ni^{2+} from single spiked aqueous solutions in batch and continuous mode. J. Colloid Interface Sci. 552:337–350. https://doi.org/10.1016/j.jcis.2019.05.046

Araya M, Olivares M, Pizarro F (2007) Copper in human health. IJEnvH 1:608–620. https://doi.org/10.1504/IJENVH.2007.018578

Barquilha CER, Cossich ES, Tavares CRG, da Silva EA (2019) Biosorption of nickel and copper ions from synthetic solution and electroplating effluent using fixed bed column of immobilized brown algae. J. Water Process Eng. 32:100904. https://doi.org/10.1016/j.jwpe.2019.100904

Bernardinelli OD, Lima MA, Rezende CA, Polikarpov I, deAzevedo ER (2015) Quantitative ^{13}C MultiCP solid-state NMR as a tool for evaluation of cellulose crystallinity index measured directly inside sugarcane biomass. Biotechnol. Biofuels 8:1–11. https://doi.org/10.1186/s13068-015-0292-1

Bohart GS, Adams EQ (1920) Some aspects of the behavior of charcoal with respect to chlorine.[1]. J. Am. Chem. Soc. 42:523–544. https://doi.org/10.1021/ja01448a018

Borgia GC, Brown RJS, Fantazzini P (1998) Uniform-penalty inversion of multiexponential decay data. J. Magn. Reson. 132:65–77. https://doi.org/10.1006/jmre.1998.1387

Boyd GE, Adamson AW, Myers LS (1947) The exchange adsorption of ions from aqueous solutions by organic zeolites. II. Kinetics1. J. Am. Chem. Soc. 69:2836–2848. https://doi.org/10.1021/ja01203a066

Brownstein KR, Tarr CE (1979) Importance of classical diffusion in NMR studies of water in biological cells. Phys. Rev. A 19:2446–2453. https://doi.org/10.1103/PhysRevA.19.2446

Bunting JW, Thong KM (1970) Stability constants for some 1:1 metal–carboxylate complexes. Can. J. Chem. 48:1654–1656. https://doi.org/10.1139/v70-273

Capitani D, Di Tullio V, Proietti N (2012) Nuclear magnetic resonance to characterize and monitor Cultural Heritage. Prog. Nucl. Mag. Res. Sp. 64:29–69. https://doi.org/10.1016/j.pnmrs.2011.11.001

Cechinel MAP, Mayer DA, Mazur LP, Silva LGM, Girardi A, Vilar VJP, de Souza AAU, de Souza Guelli U, SMA, (2018) Application of ecofriendly cation exchangers (*Gracilaria caudata* and *Gracilaria cervicornis*) for metal ions separation and recovery from a synthetic petrochemical wastewater: Batch and fixed bed studies. J. Clean. Prod. 172:1928–1945. https://doi.org/10.1016/j.jclepro.2017.11.235

Chu KH (2010) Fixed bed sorption: Setting the record straight on the Bohart-Adams and Thomas models. J. Hazard. Mater. 177:1006–1012. https://doi.org/10.1016/j.jhazmat.2010.01.019

Członkowska A, Litwin T, Dusek P, Ferenci P, Lutsenko S, Medici V, Rybakowski JK, Weiss KH, Schilsky ML (2018) Wilson disease. Nat Rev Dis Primers 4:1–20. https://doi.org/10.1038/s41572-018-0018-3

Dean JA, Lange NA (1999) Lange's Handbook of chemistry. McGraw-Hill, New York

Do D (1998) Adsorption analysis: equilibria and kinetics. Adsorption Analysis: Equilibria and Kinetics. Imperial College Press, London

Elias MMC, Ferreira GMD, de Almeida FTR, Rosa NCM, Silva IA, Filgueiras JG, de Azevedo ER, da Silva LHM, Melo TMS, Gil LF, Gurgel LVA (2019) Synthesis and application of sugarcane bagasse cellulose mixed esters. Part I: Removal of Co^{2+} and Ni^{2+} from single spiked aqueous solutions in batch mode using sugarcane bagasse cellulose succinate phthalate. J Colloid Interf Sci 533:678–691. https://doi.org/10.1016/j.jcis.2018.08.109

Fetter CW (2018) Applied Hydrogeology, 4th edn. Waveland Press, Illinois

Freitas ED, de Almeida HJ, Vieira MGA (2017) Binary adsorption of zinc and copper on expanded vermiculite using a fixed bed column. Appl Clay Sci 146:503–509. https://doi.org/10.1016/j.clay.2017.07.004

Garrels RM, Christ CL (1965) Solutions, minerals, and equilibrium. Freeman. Harper and Row, New York

Georgin J, Franco D, Drumm FC, Grassi P, Netto MS, Allasia D, Dotto GL (2020) Powdered biosorbent from the mandacaru cactus (cereus jamacaru) for discontinuous and continuous removal of Basic Fuchsin from aqueous solutions. Powder Technol. 364:584–592. https://doi.org/10.1016/j.powtec.2020.01.064

Guibal E, Milot C, Tobin JM (1998) Metal-anion sorption by chitosan beads: equilibrium and kinetic studies. Ind Eng Chem Res 37:1454–1463. https://doi.org/10.1021/IE9703954

Guo XY, Liang S, Tian QH (2011) Removal of heavy metal ions from aqueous solutions by adsorption using modified orange peel as adsorbent. Adv Mat Res 236–238:237–240. https://doi.org/10.4028/www.scientific.net/AMR.236-238.237

Gurgel LV, Junior OK, Gil RP, Gil LF (2008) Adsorption of Cu(II), Cd(II), and Pb(II) from aqueous single metal solutions by cellulose and mercerized cellulose chemically modified with succinic anhydride. Bioresour Technol 99:3077–83. https://doi.org/10.1016/j.biortech.2007.05.072

Hameed BH, El-Khaiary MI (2008) Batch removal of malachite green from aqueous solutions by adsorption on oil palm trunk fibre: equilibrium isotherms and kinetic studies. J Hazard Mater 154:237–244. https://doi.org/10.1016/j.jhazmat.2007.10.017

Harripersadth C, Musonge P, Makarfi Isa Y, Morales MG, Sayago A (2020) The application of eggshells and sugarcane bagasse as potential biomaterials in the removal of heavy metals from aqueous solutions. S Afr J Chem Eng 34:142–150. https://doi.org/10.1016/j.sajce.2020.08.002

Haynes WM, Lide DR, Bruno TJ (2014) CRC Handbook of Chemistry and Physics. Taylor & Francis, Boca Raton

Homagai PL, Ghimire KN, Inoue K (2010) Adsorption behavior of heavy metals onto chemically modified sugarcane bagasse. Bioresour Technol 101:2067–2069. https://doi.org/10.1016/j.biortech.2009.11.073

Huckel E, Debye P (1923) The theory of electrolytes. I. Lowering of freezing point and related phenomena. Phys Z 24:185–206

Júnior OK, Gurgel LVA, de Freitas RP, Gil LF (2009) Adsorption of Cu(II), Cd(II), and Pb(II) from aqueous single metal solutions by mercerized cellulose and mercerized sugarcane bagasse chemically modified with EDTA dianhydride (EDTAD). Carbohydr. Polym. 77:643–650. https://doi.org/10.1016/j.carbpol.2009.02.016

Kumar S, Prasad S, Yadav KK, Shrivastava M, Gupta N, Nagar S, Bach Q-V, Kamyab H, Khan SA, Yadav S, Malav LC (2019) Hazardous heavy metals contamination of vegetables and food chain: role of sustainable remediation approaches - A review. Environ. Res. 179:108792. https://doi.org/10.1016/j.envres.2019.108792

Langmuir I (1918) The adsorption of gases on plane surfaces of glass, mica and platinum. J. Am. Chem. Soc. 40:1361–1403. https://doi.org/10.1021/ja02242a004

Li Y, Zhou Q, Ren B, Luo J, Yuan J, Ding X, Bian H, Yao X (2019) Trends and health risks of dissolved heavy metal pollution in Global River and Lake Water from 1970 to 2017. In: de Voogt P (ed) Reviews of Environmental Contamination and Toxicology. Springer International Publishing, Cham, pp 1–24

Liu Y (2009) Is the free energy change of adsorption correctly calculated? J. Chem. Eng. Data 54:1981–1985. https://doi.org/10.1021/je800661q

Liu CC, Li YS, Chen YM, Wang MK, Chiou CS, Yang CY, Lin YA (2011) Biosorption of chromium, copper and zinc on rice wine processing waste sludge in fixed bed. Desalination 267:20–24. https://doi.org/10.1016/j.desal.2010.08.040

Lu C, Xiao-Kun L, Ye S, Cherian MG (2005) Essentiality, toxicology and chelation therapy of zinc and copper. Curr. Med. Chem. 12:2753–2763. https://doi.org/10.2174/092986705774462950

Maheshwari U, Gupta S (2016) Performance evaluation of activated neem bark for the removal of Zn(II) and Cu(II) along with other metal ions from aqueous solution and synthetic pulp & paper industry effluent using fixed-bed reactor. Process Saf. Environ. Prot. 102:547–557. https://doi.org/10.1016/j.psep.2016.05.009

Malash GF, El-Khaiary MI (2010) Piecewise linear regression: a statistical method for the analysis of experimental adsorption data by the intraparticle-diffusion models. Chem. Eng. J. 163:256–263. https://doi.org/10.1016/j.cej.2010.07.059

Marcus Y (1994) A simple empirical model describing the thermodynamics of hydration of ions of widely varying charges, sizes, and shapes. Biophys. Chem. 51:111–127. https://doi.org/10.1016/0301-4622(94)00051-4

McMurray J, Fay RC (2004) Chemistry. Pearson Education Inc., Prentice Hall

Melo JCP, Silva Filho EC, Santana SAA, Airoldi C (2011) Synthesized cellulose/succinic anhydride as an ion exchanger. Calorimetry of divalent cations in aqueous suspension. Thermochim. Acta 524:29–34. https://doi.org/10.1016/j.tca.2011.06.007

Meng X, Ragauskas AJ (2014) Recent advances in understanding the role of cellulose accessibility in enzymatic hydrolysis of lignocellulosic substrates. Curr. Opin. Biotech. 27:150–158. https://doi.org/10.1016/j.copbio.2014.01.014

Mitchell J, Stark SC, Strange JH (2005) Probing surface interactions by combining NMR cryoporometry and NMR relaxometry. J Phys D Appl Phys 38:1950. https://doi.org/10.1088/0022-3727/38/12/015

Nightingale ER (1959) Phenomenological Theory of ion solvation. Effective Radii of Hydrated Ions. J Phys Chem 63:1381–1387. https://doi.org/10.1021/j150579a011

O'Connell DW, Birkinshaw C, O'Dwyer TF (2008) Heavy metal adsorbents prepared from the modification of cellulose: a review. Bioresour Technol 99:6709–6724. https://doi.org/10.1016/j.biortech.2008.01.036

Pavia D, Lampman G, Kriz G, Vyvyan J (2009) Introduction to Spectroscopy. Cengage Learning, Belmont, USA

Pearson RG (1963) Hard and Soft Acids and Bases. J. Am. Chem. Soc. 85:3533–3539. https://doi.org/10.1021/ja00905a001

Pearson RG (1968) Hard and soft acids and bases, HSAB, part 1: Fundamental principles. J. Chem. Educ. 45:581–587. https://doi.org/10.1021/ed045p581

Pereira AR, Soares LC, Teodoro FS, Elias MMC, Ferreira GMD, Savedra RML, Siqueira MF, Martineau-Corcos C, da Silva LHM, Prim D, Gurgel LVA (2020) Aminated cellulose as a versatile adsorbent for batch removal of As(V) and Cu(II) from mono- and multicomponent aqueous solutions. J. Colloid Interface Sci. 576:158–175. https://doi.org/10.1016/j.jcis.2020.04.129

Prasad R, Srivastava S (2009) Sorption of distillery spent wash onto fly ash: kinetics and mass transfer studies. Chem. Eng. J. 146:90–97. https://doi.org/10.1016/j.cej.2008.05.021

Provencher SW (1982) CONTIN: A general purpose constrained regularization program for inverting noisy linear algebraic and integral equations. Comput. Phys. Commun. 27:229–242. https://doi.org/10.1016/0010-4655(82)90174-6

Ramos SNC, Xavier ALP, Teodoro FS, Elias MMC, Gonçalves FJ, Gil LF, de Freitas RP, Gurgel LVA (2015) Modeling mono- and multicomponent adsorption of cobalt(II), copper(II), and nickel(II) metal ions from aqueous solution onto a new carboxylated sugarcane bagasse. Part I: Batch adsorption study. Ind. Crops. Prod. 74:357–371. https://doi.org/10.1016/j.indcrop.2015.05.022

Ramos SNC, Xavier ALP, Teodoro FS, Gil LF, Gurgel LVA (2016) Removal of cobalt(II), copper(II), and nickel(II) ions from aqueous solutions using phthalate-functionalized sugarcane bagasse: mono- and multicomponent adsorption in batch mode. Ind. Crops. Prod. 79:116–130. https://doi.org/10.1016/j.indcrop.2015.10.035

Rezende CA, de Lima MA, Maziero P, deAzevedo ER, Garcia W, Polikarpov I (2011) Chemical and morphological characterization of sugarcane bagasse submitted to a delignification process for enhanced enzymatic digestibility. Biotechnol. Biofuels 4:1–19. https://doi.org/10.1186/1754-6834-4-54

Salomons W, Förstner U, Mader P (1995) Heavy metals: problems and solutions. Springer-Verlag, Berlin, Germany

Saravanan A, Jeevanantham S, Senthil Kumar P, Varjani S, Yaashikaa PR, Karishma S (2020) Enhanced Zn(II) ion adsorption on surface modified mixed biomass – Borassus flabellifer and Aspergillus tamarii: Equilibrium, kinetics and thermodynamics study. Ind. Crops. Prod. 153:112613. https://doi.org/10.1016/j.indcrop.2020.112613

Shanmugaprakash M, Venkatachalam S, Rajendran K, Pugazhendhi A (2018) Biosorptive removal of Zn(II) ions by Pongamia oil cake (Pongamia pinnata) in batch and fixed-bed column studies using response surface methodology and artificial neural network. J. Environ. Manage. 227:216–228. https://doi.org/10.1016/j.jenvman.2018.08.088

Sips R (1948) On the structure of a catalyst surface. J. Chem. Phys. 16:490–495. https://doi.org/10.1063/1.1746922

Tang J, Zhang J, Ren L, Zhou Y, Gao J, Luo L, Yang Y, Peng Q, Huang H, Chen A (2019) Diagnosis of soil contamination using microbiological indices: a review on heavy metal pollution. J. Environ. Manage. 242:121–130. https://doi.org/10.1016/j.jenvman.2019.04.061

Taylor AA, Tsuji JS, Garry MR, McArdle ME, Goodfellow WL, Adams WJ, Menzie CA (2020) Critical review of exposure and effects: implications for setting regulatory health criteria for ingested copper. Environ. Manage. 65:131–159. https://doi.org/10.1007/s00267-019-01234-y

Teodoro FS, Ramos SNC, Elias MMC, Mageste AB, Ferreira GMD, da Silva LHM, Gil LF, Gurgel LVA (2016) Synthesis and application of a new carboxylated cellulose derivative. Part I: Removal of Co^{2+}, Cu^{2+} and Ni^{2+} from monocomponent spiked aqueous solution. J. Colloid Interface Sci. 483:185–200. https://doi.org/10.1016/j.jcis.2016.08.004

Thomas HC (1944) Heterogeneous ion exchange in a flowing system. J. Am. Chem. Soc. 66:1664–1666. https://doi.org/10.1021/ja01238a017

Tsuchida JE, Rezende CA, de Oliveira-Silva R, Lima MA, d'Eurydice MN, Polikarpov I, Bonagamba TJ (2014) Nuclear magnetic resonance investigation of water accessibility in cellulose of pretreated sugarcane bagasse. Biotechnol. Biofuels 7:1–13. https://doi.org/10.1186/s13068-014-0127-5

Upadhyay U, Sreedhar I, Singh SA, Patel CM, Anitha KL (2021) Recent advances in heavy metal removal by chitosan based adsorbents. Carbohydr. Polym. 251:117000. https://doi.org/10.1016/j.carbpol.2020.117000

Vázquez G, Calvo M, Sonia Freire M, González-Alvarez J, Antorrena G (2009) Chestnut shell as heavy metal adsorbent: optimization study of lead, copper and zinc cations removal. J. Hazard. Mater. 172:1402–1414. https://doi.org/10.1016/j.jhazmat.2009.08.006

Viegas RMC, Campinas M, Costa H, Rosa MJ (2014) How do the HSDM and Boyd's model compare for estimating intraparticle diffusion coefficients in adsorption processes. Adsorption 20:737–746. https://doi.org/10.1007/s10450-014-9617-9

Weber WJ, Morris JC (1963) Kinetics of adsorption on carbon from solution. J. Sanit. Eng. Div. 89:31–60

Worch E (2012) Adsorption technology in water treatment: fundamentals, process, and modeling. de Gruyter, Berlin

Xavier ALP, Adarme OFH, Furtado LM, Ferreira GMD, da Silva LHM, Gil LF, Gurgel LVA (2018) Modeling adsorption of copper(II), cobalt(II) and nickel(II) metal ions from aqueous solution onto a new carboxylated sugarcane bagasse. Part II: Optimization of monocomponent fixed-bed column adsorption. J. Colloid Interf. Sci. 516:431–445. https://doi.org/10.1016/j.jcis.2018.01.068

Yu J-x, Wang L-y, Chi R-a, Zhang Y-f, Xu Z-g, Guo J (2015) Adsorption of Pb^{2+}, Cd^{2+}, Cu^{2+}, and Zn^{2+} from aqueous solution by modified sugarcane bagasse. Res. Chem. Intermed. 41:1525–1541. https://doi.org/10.1007/s11164-013-1290-1